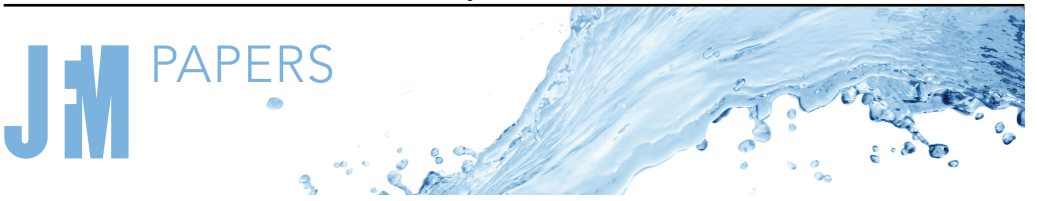
J. Fluid Mech. (2026), *vol.* 1043, A45, doi:10.1017/jfm.2026.12073



Drag reduction and subcritical turbulence in controlled pipe flows

Emanuele Gallorini[1,2], **Daniele Massaro**[3], **Philipp Schlatter**[4] and **Maurizio Quadrio**[1]

[1]Dipartimento di Scienze e Tecnologie Aerospaziali, Politecnico di Milano, via La Masa 34, Milano 20156, Italy

[2]Univ. Lille, CNRS, ONERA, Arts et Metiers Institute of Technology, Centrale Lille, UMR 9014 – LMFL – Laboratoire de Mécanique des Fluides de Lille – Kampé de Fériet, Lille 59000, France

[3]Department of Mechanical Engineering, Massachusetts Institute of Technology, 77 Massachusetts Avenue, Cambridge, 02139 MA, USA

[4]Institute of Fluid Mechanics (LSTM), Friedrich–Alexander–Universität (FAU) Erlangen–Nürnberg, Erlangen 91058, Germany

Corresponding author: Emanuele Gallorini, emanuele.gallorini@polimi.it

(Received 17 April 2026 UTC; revised 28 July 2026 UTC; accepted 31 August 2026 UTC)

Pipe flow controlled by streamwise-travelling waves of azimuthal wall velocity is studied using direct numerical simulations at a bulk Reynolds number $Re_b = 4900$. A comprehensive analysis of drag reduction shows that the flow response differs fundamentally from that of channel flow. Under suitable forcing, pipe flow relaminarises, whereas channel flow does not. Depending on the control parameters, the flow exhibits the spatially localised turbulent state characteristic of transitional pipe flow, with turbulent puffs persisting at bulk Reynolds numbers up to three times higher than in the uncontrolled case. The bulk Reynolds number alone does not determine the onset of localisation. Moreover, drag reduction, which alters the natural relation between bulk and friction velocities, is insufficient to identify a universal onset criterion. An intermittency indicator based on the spatial variance of the cross-sectional turbulent kinetic energy relates the emergence of localised turbulence to the low wall friction produced by the control, although the correspondence is not one-to-one. Despite their qualitative resemblance to canonical turbulent puffs, the controlled puffs exhibit distinct properties; for example, their fronts may propagate faster than the bulk flow. Overall, this work provides a comprehensive characterisation of the subcritical turbulent state and its turbulent puffs in controlled pipe flow, and offers a new perspective on control strategies that aim at flow relaminarisation.

Key words: drag reduction

© The Author(s), 2026. Published by Cambridge University Press.

https://doi.org/10.1017/jfm.2026.12073 Published online by Cambridge University Press

1. Introduction

Controlling turbulent flows for drag reduction remains an active area of research, driven by its economic and environmental relevance. For parallel flows, where only friction drag is present, the open-loop control strategy based on streamwise-travelling waves of spanwise wall velocity is known to be effective at reducing turbulent skin-friction drag and producing large net savings (Quadrio *et al.* 2009). This method imposes a distribution of spanwise velocity at the wall, which varies with the streamwise position and time (see Ricco *et al.* 2021 for an in-depth review). Streamwise-traveling waves (STWs) have proved their drag-reduction abilities at high Re (Gatti *et al.* 2025) and in compressible flows (Gattere *et al.* 2024; Ruby & Foysi 2025); for non-canonical flows, STWs have been applied to a transonic wing, yielding large improvements in the aerodynamic efficiency (Berizzi *et al.* 2025). STWs have also been found to improve the stability characteristics of the channel flow, delaying transition (Massaro *et al.* 2023).

STWs are primarily studied in plane channel flow. Although pipes are common in applications, circular pipe flow remains far less studied. A comprehensive characterisation of STW performance in pipe flow is not yet available and is therefore one of the goals of the current work. Quadrio & Sibilla (2000) studied uniform wall oscillation, which represents the limit case of a travelling wave with infinite wavelength, in a pipe and determined its potential for drag reduction. Liu *et al.* (2022) considered a stationary wave by changing the control amplitude and wavelength. Recently, the drag-reducing potential of a purely rotating pipe (i.e. wave with infinite wavelength and oscillation period) was assessed by Xiao *et al.* (2024). The first experimental investigation of STWs was carried out in the pipe geometry by Auteri *et al.* (2010) at the same Re as the original numerical study by Quadrio *et al.* (2009), namely $Re_b = 4900$, where $Re_b = U_b D/\nu$, with D the pipe diameter, U_b the bulk velocity and ν the kinematic viscosity. Their actuation device, based on independently rotating slabs, implemented a spatially discrete analogue of travelling waves, and two forcing wavelengths were examined. Recently, Gallorini & Quadrio (2024) performed direct numerical simulations (DNS) of the same pipe flow controlled with discrete STWs. To enable a direct comparison, they kept the same relatively low Re_b of the experiment, and discussed how differences between experiments and simulations (previously available for the planar geometry only) are caused by the spatially discrete waveform of the azimuthal forcing. An important additional difference was identified: depending on the control parameters, the flow in the simulation may either fully relaminarise or develop spatially localised turbulence.

Hence, beyond the obvious interest in drag-reduction data for the relatively unexplored pipe geometry, this study examines drag-reduced flows at low Reynolds numbers, offering a unique perspective on the transition to turbulence in a controlled pipe flow. The occurrence of localised turbulence at $Re_b = 4900$ is, in fact, unexpected, as this value far exceeds the value of the critical Reynolds number $Re_c = 2040$ reported by Avila *et al.* (2011) for the onset of localised turbulence in canonical pipe flow. Pipe flow transition has been studied intensively since the pioneering experiments of Reynolds (1883), yet some aspects remain a matter of debate. In canonical pipe flow, transition is subcritical: the Hagen–Poiseuille parabolic velocity profile is stable to infinitesimal perturbations for any value of Re (Schmid & Henningson 2001). Numerical simulations have indeed shown that laminar pipe flow disturbed by infinitesimal perturbations remains stable up to $Re = 10^7$ (Meseguer & Trefethen 2003). Experiments, however, have not reported laminar flow at such high Reynolds numbers (van Doorne & Westerweel 2008), indicating that pipe flow transition is triggered by finite-amplitude disturbances. During transition to turbulence, these localised structures proliferate: their average growth rate increases with Re, first

https://doi.org/10.1017/jfm.2026.12073 Published online by Cambridge University Press

exceeding their decay rate, so that puffs are surrounded by laminar flow (Avila *et al.* 2011), and eventually, at higher Re, conventional space-filling turbulence is obtained (Moxey & Barkley 2010; Avila & Hof 2013).

The Reynolds number Re_b determines the boundary between growing and decaying puffs and marks the onset of turbulence. Isolated puffs have been observed at $Re_b \approx 1500$ (Hof *et al.* 2005). At higher Re_b, the turbulent clusters expand at a rate that, after the initial formation time, is independent of Re_b (Barkley *et al.* 2015); these are called slugs (Lindgren 1957; Wygnanski & Champagne 1973). Puffs have coherent features, travel at a speed slightly smaller than U_b, and have a well-defined streamwise length, independent of the details of the disturbance that creates them. They emerge sharply from the quiet, laminar state at their upstream side, whereas the laminar state downstream recovers slowly. Over recent decades, turbulent puffs have been characterised in detail both experimentally and numerically (see Avila *et al.* 2023 and references herein). Wygnanski *et al.* (1975) experimentally studied pipe flow transition in the range $2000 \leqslant Re_b \leqslant 2700$ and observed non-decaying puffs, regardless of the initial perturbation, and therefore, self-sustained turbulence at $Re_b \geqslant 2200$. Whether turbulent puffs cease to decay at a well-defined critical Reynolds number or remain inherently transient at low Re_b is an ongoing debate. Experiments (Peixinho & Mullin 2006) and numerical simulations (Willis & Kerswell 2007) have found that turbulent puffs relaminarise at low Re_b, showing a power-law scaling of the transient decay half-life and suggesting a boundary crisis. At the same time, Hof *et al.* (2006) suggested a different scenario, noting that the characteristic time of a turbulent puff does not diverge; instead, it increases exponentially with the Reynolds number, as numerically pointed out by Faisst & Eckhardt (2004) up to $Re_b = 2100$. This finding was later confirmed both experimentally (Hof *et al.* 2008; de Lozar & Hof 2009) and numerically (Avila *et al.* 2010). Determining the critical value Re_c of the Reynolds number at which turbulence becomes sustained has been a long-standing challenge. Initially, Re_c was defined as the point where the lifetime of a turbulent cluster diverges. Later, proliferation/splitting processes were identified as the key mechanism leading to sustained turbulence (Moxey & Barkley 2010) and, by comparing the characteristic time scales of puff decay and splitting, Avila *et al.* (2011) identified a critical Reynolds number $Re_c = 2040$ at which the decay and splitting time scales are equal. This finding was later confirmed by Mukund & Hof (2018), who demonstrated that puffs relaminarise for $Re_b < 2020$, while turbulence becomes sustained for $Re_b > 2060$.

In the studies discussed above, the onset of transition in pipe flow is universally characterised by the bulk Reynolds number Re_b. In canonical pipe flow, a given value of Re_b corresponds to a unique Kármán number R^+, defined as $R^+ = Ru_\tau/\nu$, where R is the pipe radius and u_τ is the friction velocity, i.e. the square root of the wall friction over the fluid density. Here R^+ is analogous to the friction Reynolds number Re_τ, which is widely used to describe plane channel flow. However, the link between Re_b and Re_τ is altered when skin-friction drag reduction lowers Re_τ for a given Re_b or, conversely, increases Re_b for a given Re_τ (Hasegawa *et al.* 2014). Therefore, the present study systematically examines the transitional and turbulent states in pipe flow with STWs, where the usual relationship between Re_b and R^+ is broken. Direct numerical simulation is used to explore a broad region of the control parameter space, with the Reynolds number fixed at $Re_b = 4900$, well above the value required for the uncontrolled flow to produce conventional, space-filling turbulence.

The paper is organised as follows. Section 2 describes the numerical methods and computational procedures used to generate the DNS dataset. An overview of the drag-reduction results is presented in § 3, followed by a discussion of the localised turbulence state in § 4. Finally, § 5 presents concluding remarks.

https://doi.org/10.1017/jfm.2026.12073 Published online by Cambridge University Press

2. Simulations

Direct numerical simulations of the flow in a cylindrical pipe are carried out by numerically integrating the incompressible Navier–Stokes equations, formulated in primitive variables and cylindrical coordinates.

The DNS solver is written in the CPL programming language (Luchini 2020, 2021) and is derived from the Cartesian solver originally introduced by Luchini & Quadrio (2006); additional details are provided in Gallorini & Quadrio (2024). The equations are written in terms of velocity $\boldsymbol{u} = (u_x, u_r, u_\theta)$ and pressure p, where u_x, u_r and u_θ denote the velocity components in the axial, radial and azimuthal directions, respectively. The periodic azimuthal and axial directions are spectrally discretised, while compact second-order finite differences are used in the radial direction. No-penetration and no-slip conditions are applied at the pipe wall. A non-homogeneous Dirichlet condition on the azimuthal velocity component is applied to prescribe the control action. Regularity conditions are imposed at the pipe axis (Lewis & Bellan 1990). The time-advancement scheme employs a partially implicit approach. The viscous term is discretised using the implicit Crank–Nicolson scheme, while the convective term is treated using the three-substep, low-storage Runge–Kutta scheme described by Rai & Moin (1991). The number of azimuthal Fourier modes is constrained by the resolution near the pipe wall. Since this would lead to unnecessarily high resolution toward the pipe axis and to a consequent severe time-step limitation, the code smoothly reduces the number of azimuthal modes as the pipe axis is approached.

The simulations are carried out at a constant flow rate, adjusting the axial pressure gradient at every time step, as described by Quadrio *et al.* (2016). Therefore, the bulk Reynolds number $Re_b = U_b D/\nu = 4900$ is constant during the simulations. For the reference (uncontrolled) turbulent pipe flow, $Re_b = 4900$ corresponds to $R^+ = 170$. Since the axial domain length L_x is one of the most critical discretisation parameters, a dedicated analysis is conducted in Appendix A, varying L_x from $8.5D$ to $122.5D$. The results indicate that $L_x \simeq 30D$ is sufficient to accurately reproduce the quantities of interest, and $L_x = 30D$ is therefore employed for the baseline set of cases. Note that $L_x = 30D$ exceeds the lengths typically used for turbulent pipe flow simulations (Kim & Adrian 1999; Wu & Moin 2008). The axial and azimuthal directions are discretised using 1364×192 Fourier modes. After dealiasing, the grid spacing is $\Delta x^+ = 5$ and $r\Delta\theta^+ = 3.7$ at the pipe wall for the uncontrolled case, where $(\cdot)^+$ indicates quantities expressed in viscous units. Note that drag reduction implies finer spatial resolution in actual viscous units. The number of azimuthal modes N_θ varies with the radial direction: it remains constant at $N_\theta = 192$ from the wall ($r = D/2$) to $r = 0.4R$, then it decreases linearly, as described by Gallorini & Quadrio (2024), to reach $N_\theta = 4$ at the pipe centreline. The radial grid spacing increases smoothly from the wall toward the pipe axis, following a hyperbolic tangent distribution: it is $\Delta r^+ = 0.7$ at the wall and $\Delta r^+ = 2.4$ at the centreline in the reference flow. The time step Δt is dynamically adjusted to ensure that the Courant–Friedrichs–Lewy (CFL) number equals unity, with an average value of $\Delta t^+ = 0.1$. Additional simulations were conducted with the smaller value CFL $= 0.5$, to confirm the absence of any noticeable difference in the results.

A large dataset is built, with more than one thousand (1184) simulations of pipe flow controlled by STWs. For all cases, the initial condition is an unforced turbulent flow in statistical equilibrium. The applied wall forcing is

$$u_\theta(x, t) = A \sin(k_x x - \omega t), \tag{2.1}$$

containing three parameters: the forcing amplitude A, the wavenumber k_x and the angular frequency ω. In this study, two of the three parameters are varied, with the amplitude

https://doi.org/10.1017/jfm.2026.12073 Published online by Cambridge University Press

fixed at $A/U_b = 1$ (or $A^+ = 14.5$), the same value used by Auteri *et al.* (2010) and Gallorini & Quadrio (2024). The baseline pipe length $L_x = 30D$ is slightly adjusted to always accommodate an integer number of waves. The simulations are run for $500D/U_b$. Statistics are computed after discarding the first half of the time history to remove the initial transient, during which the flow adjusts to the controlled state. For the analyses described in § 4.2 and Appendix A.1, results are obtained by averaging over instantaneous velocity fields saved over a time window of $tU_b/D = 250$ after eliminating the transient.

Results are made dimensionless either in external units (with U_b and D as the velocity and length scales) or in inner units (with u_τ and ν/u_τ). Since U_b is fixed, drag reduction changes the value of u_τ. The superscript $(\cdot)^+$ is used for quantities expressed in friction units of the uncontrolled case, whereas the superscript $(\cdot)^*$ indicates scaling based on the actual friction velocity of the controlled case.

Several averaging operators are employed. Here $\langle u\rangle(r)$ indicates the average of the field $u(x, r, \theta, t)$ over time and the two homogeneous directions

$$\langle u\rangle(r) = \frac{1}{2\pi L_x T}\int_0^T\int_0^{L_x}\int_0^{2\pi} u(x, r, \theta, t)\,\mathrm{d}\theta\mathrm{d}x\mathrm{d}t, \tag{2.2}$$

where the time is measured after discarding the transient. Similarly, we define the azimuthal average at time t as

$$\langle u\rangle_\theta(x, r, t) = \frac{1}{2\pi}\int_0^{2\pi} u(x, r, \theta, t)\,\mathrm{d}\theta. \tag{2.3}$$

The notation $\langle u\rangle_p(r)$ indicates the average of $u(x, r, \theta, t)$ inside a puff, i.e. within an instantaneous turbulent structure as defined in § 4. If a structure is defined with a local streamwise axis x' such that its extension ranges from $x' = 0$ to $x' = \ell(t)$, the puff-averaged axial velocity is

$$\langle u\rangle_p(r) = \frac{1}{2\pi \ell T}\int_0^T\int_0^{\ell}\int_0^{2\pi} u(x', r, \theta, t)\,\mathrm{d}\theta\mathrm{d}x'\mathrm{d}t. \tag{2.4}$$

The availability of a puff-averaged friction velocity implies that, besides the $*$ scaling built with the actual-global friction velocity, an additional actual-local scaling can be used, which will be indicated with a double asterisk superscript, namely $(\cdot)^{**}$.

3. Drag reduction

This section presents the drag-reduction performance of STWs in pipe flow, which is still missing as outlined in § 1. The current dataset is designed to cover very low streamwise wavenumbers, since information on this region of parameter space is quite limited for the plane channel case, owing to the high computational cost. The dataset includes cases in which k_x corresponds to a forcing wavelength of up to $27D$. For comparison, channel flow studies typically use domains with streamwise lengths of about $L_x \approx 6D$ (interpreting D as the gap between the two walls).

The drag-reduction rate $\mathcal{R}$ is quantified by the percentage change in the friction coefficient C_f as

$$\mathcal{R} = 100\left(1 - \frac{C_f}{C_{f,0}}\right), \tag{3.1}$$

https://doi.org/10.1017/jfm.2026.12073 Published online by Cambridge University Press

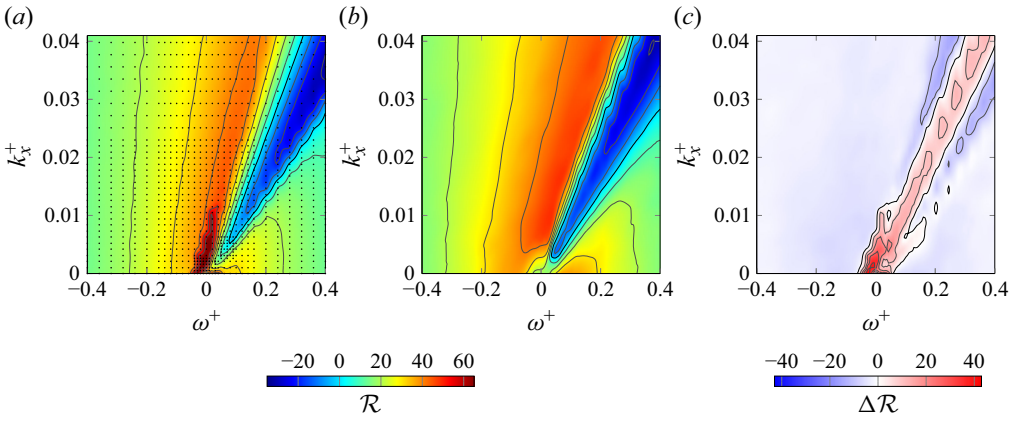


Figure 1. Maps of the percentage drag-reduction rate $\mathcal{R}$ in the $\omega - k_x$ plane for $A^+ = 14.5$. Present results (*a*) are compared with plane channel flow data (*b*), extrapolated from $Re_\tau = 200$ to $Re_\tau = 170$. Contours are spaced by 10 % intervals; the thick line indicates the zero contour level. Panel (*c*) shows the difference $\Delta\mathcal{R}$ between pipe and channel. In panel (*a*) the dots show where simulations have been carried out.

where the subscript $(\cdot)_0$ refers to quantities computed for the reference case. The coefficient C_f is defined as

$$C_f = \frac{2\tau_w}{\rho U_b^2}, \tag{3.2}$$

where τ_w is the mean streamwise shear stress at the pipe wall, i.e.

$$\tau_w = -\mu \frac{\partial \langle u_x \rangle}{\partial r}\bigg|_{r=D/2} \tag{3.3}$$

and μ is the dynamic viscosity. Figure 1 provides an overview of $\mathcal{R}$ in the (ω^+, k_x^+) plane, in comparative form between the channel and pipe. The dots on the map in panel (*a*) indicate the frequency–wavenumber combinations at which the pipe flow simulations are carried out. Regions where drag-reduction rates exhibit strong gradients, particularly near the transition between drag reduction and drag increase at low k_x^+, are locally refined by adding sampling points. Note that the point at $\omega^+ = 0$ and $k_x^+ = 0$ represents a wave with infinite period and wavelength, therefore, a uniformly rotating pipe, which in principle produces drag reduction (Xiao *et al.* 2024). Per the definition of (2.1), the rotation velocity is $u_\theta(x, t) = A \sin(0) = 0$ in our case, corresponding to a motionless pipe, hence $\mathcal{R} = 0$. The cylindrical case differs from the planar one, where a uniform wall velocity may result, depending on the motion law for the wall, in the two walls moving in the same or in opposite directions. For comparison, the panel (*b*) shows $\mathcal{R}$ for a plane channel at $A^+ = 14.5$, obtained by extrapolating the dataset of Gatti & Quadrio (2016) at $Re_\tau = 200$. The effect of the spanwise forcing can be converted into a Reynolds-independent measure, i.e. the shift ΔB^+ of the logarithmic layer of the mean velocity profile

$$\Delta B^+ = \sqrt{\frac{2}{C_{f,0}}}[(1 - \mathcal{R}/100)^{-1/2} - 1] - \frac{1}{2\kappa} \ln(1 - \mathcal{R}/100), \tag{3.4}$$

where κ is the von Kármán constant. By solving (3.4) and knowing ΔB^+, the value of $\mathcal{R}$ can be derived. The friction coefficient $C_{f,0}$ of the uncontrolled flow is the only term from (3.4) that depends on the Reynolds number. Its value has been obtained with a channel

https://doi.org/10.1017/jfm.2026.12073 Published online by Cambridge University Press

flow simulation at $Re_\tau = 170$, corresponding to $Re_b \approx 5300$, while a value of $\kappa = 0.41$ has been used for the von Kármán constant.

The map is, as expected, qualitatively similar to that of plane channel flow at the same Reynolds number. A quantitative comparison reveals higher drag reduction in the pipe flow, where a maximum of $\mathcal{R} \approx 65\,\%$ is reached, compared with $\approx 51\,\%$ in the channel. Note that $\mathcal{R} \approx 65\,\%$ represents the theoretical maximum at this Reynolds number, achieved only after complete relaminarisation. When laminarisation occurs, drag reduction cannot be interpreted in terms of a shift of the logarithmic layer of the mean velocity profile. Existing literature confirms that turbulent pipe flow tends to relaminarise more readily than channel flow (Liu *et al.* 2022), a difference that may be related to different stability properties of the base flow controlled with different control parameters. A second observation is that the region of largest $\mathcal{R}$ in the pipe shifts toward lower wavenumbers, extending down to the $k_x = 0$ axis where the forcing is purely temporal (oscillating pipe). While $\mathcal{R}$ is symmetric along the horizontal axis, for very small k_x, the left quadrant (backward-travelling waves) exhibits higher drag reduction, as in the plane channel. The drag-increasing region has a triangular shape in both cases. For the pipe, the vertex of the triangle defined by the zero contour level is at $\omega^+ \approx 0.075$ and $k_x^+ \approx 0.005$, which is slightly shifted away from the origin than in the plane channel. This position is consistent with the larger $\mathcal{R}$ in the pipe at low wavenumbers. The maximum drag increase observed across the examined range of parameters is 35 % in the pipe, compared with 30 % in the plane channel. The drag-increase triangular region is centred on a phase speed of approximately $10u_\tau$, in agreement with the original observation by Quadrio *et al.* (2009) that linked this phase speed to the average convection velocity of near-wall turbulent fluctuations and the turbulence structures sustaining them. In figure 1(*c*) we plot the difference $\Delta\mathcal{R}$ in drag-reduction rates between the pipe and channel. Since the channel flow data result from an extrapolation procedure, we expect the $\Delta\mathcal{R}$ map to capture qualitative differences and highlight the regions where differences are most significant, rather than providing their exact quantification. Despite the overall similarity, local differences can be substantial, reaching over 40 %. These large differences are concentrated near the origin of the plane, where laminarisation occurs in the pipe flow.

Interestingly, outside of the high-$\mathcal{R}$ region, the channel flow shows higher drag reduction and lower drag increase than the pipe. To rule out any unintended effect of extrapolating the plane-geometry data in the dataset of Gatti & Quadrio (2016), we carried out an additional simulation for the plane channel flow at exactly the same $Re_\tau = 170$. For the parameter values $k_x^+ = 0.02$, $A^+ = 14.5$ and $\omega^+ = -0.2$, the resulting $\mathcal{R} = 24\,\%$ is consistent with the value from (3.4) ($\mathcal{R} = 23\,\%$) and, compared with $\mathcal{R} = 22\,\%$ in the controlled pipe flow, confirms the slightly larger effectiveness of STWs at high frequencies in the planar geometry. Given the vicinity of the two values of $\mathcal{R}$, we computed the statistical uncertainty δR with the procedure described in Appendix A.1, finding a value of $\delta R = 0.6\,\%$ for the channel and $\delta R = 0.4\,\%$ for the pipe, which indicates that the difference $\Delta\mathcal{R}$ is statistically significant.

Since STW is an active technique and requires power to operate, the comparison between pipe and channel flows should be extended to consider the net power budget. The net saving $\mathcal{S}$ is computed by accounting for the control power $\mathcal{P}_{in}$, i.e. the power cost required to obtain $\mathcal{R}$,

$$\mathcal{S} = \mathcal{R} - \mathcal{P}_{in}, \tag{3.5}$$

where $\mathcal{P}_{in}$ is the input power that an ideal control system transfers to the flow, normalised by the pumping power P_0:

https://doi.org/10.1017/jfm.2026.12073 Published online by Cambridge University Press

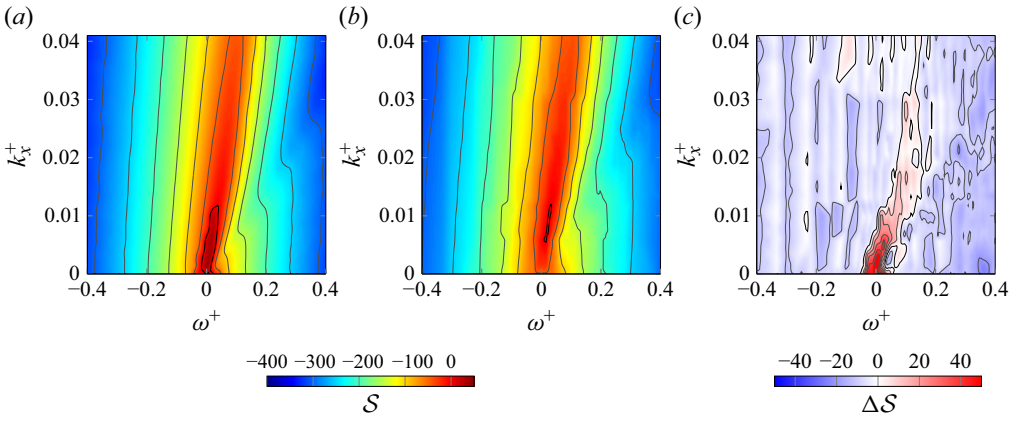


Figure 2. Maps of the net power saving $\mathcal{S}$ in the $\omega - k_x$ plane for $A^+ = 14.5$. Present results (a) are compared with plane channel flow data (b), extrapolated from $Re_\tau = 200$ to $Re_\tau = 170$. Contours are spaced by unit intervals; the thick line indicates the zero level. Panel (c) shows the difference $\Delta\mathcal{S}$ between pipe and channel.

$$\mathcal{P}_{in} = \frac{\mu}{P_0}\left\langle \left[u_\theta \left(\frac{\partial u_\theta}{\partial r} - \frac{u_\theta}{r} \right) \right]_{r=D/2} \right\rangle. \tag{3.6}$$

Figure 2 compares the map of $\mathcal{S}$ for the pipe and for the plane channel flow. Channel data are computed, following Ricco & Quadrio (2008), under the assumption that the change in friction only affects U_b^+. The power spent then becomes $\mathcal{P}_{in} \propto (U_b^+)^2$, and empirical correlations yield $U_b^+ = 0.5 Re_b/Re_\tau = 7.715 Re_\tau^{0.136}$. Note that the control amplitude used here is relatively large and differs from the amplitude that yields maximum net savings for the channel flow, which is approximately $A^+ \approx 6$ (Gatti & Quadrio 2016). Therefore, a positive net saving is nearly absent (4 %) in the plane channel case, while for pipe flow, the area with $\mathcal{S} > 0$ is wider and the maximum $\mathcal{S}$ is higher (28 %) because of laminarisation. The reliability of these findings is reinforced by the additional simulation for the plane channel flow at $k_x^+ = 0.02$ and $\omega^+ = -0.2$, which gives a net saving of $\mathcal{S} = -200$ %, compared with -220 % for the pipe flow, in agreement with the trend of figure 2. We stress again, however, that the channel flow data derive from extrapolation, and therefore, such comparisons should be interpreted qualitatively. For example, the P_{in} obtained for the channel flow DNS at $k_x^+ = 0.02$ and $\omega^+ = -0.2$ differs from the extrapolated value by 4 %. We have also confirmed that the trends discussed here for both $\Delta\mathcal{R}$ and $\Delta\mathcal{S}$ remain valid when actual viscous scaling is used instead of the viscous scaling based on the friction velocity of the uncontrolled case.

Relaminarisation by STWs in pipe flow is further discussed by presenting the local wall friction in figure 3 for two relaminarised cases. The figure shows the instantaneous local value of the Kármán number $\langle R^+ \rangle_\theta(x) = \langle (D/2)(-(1/\nu)(\partial u/\partial r)|_{r=D/2})^{1/2} \rangle_\theta$. An evident streamwise modulation of the flow is observed neither in the plane counterpart nor in the purely oscillating pipe (Coxe *et al.* 2022). For a laminar flow in a plane channel, it was shown by Quadrio & Ricco (2011) that the spanwise motion of the generalised Stokes layer decouples from the streamwise one, and therefore, the wall slope of the streamwise velocity profile does not vary with x. For laminar flow in a pipe, however, the Navier–Stokes equations written in cylindrical coordinates show that the viscous terms become coupled. Therefore, under STWs with $k_x \neq 0$, the laminar solution depends

https://doi.org/10.1017/jfm.2026.12073 Published online by Cambridge University Press

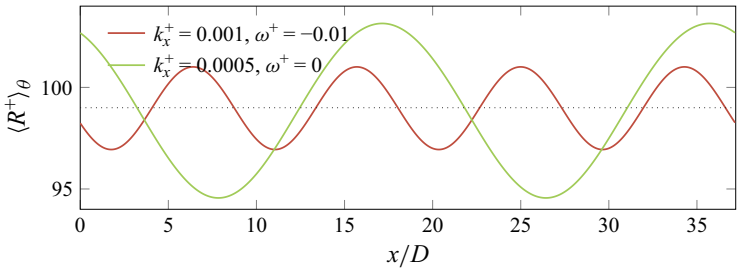


Figure 3. Local wall friction $\langle R^+ \rangle_\theta$ for different control parameters resulting in a full laminarisation of the flow. The dotted line indicates the friction level for the unforced laminar flow.

on time, wall-normal (radial) and streamwise coordinates, while remaining azimuthally homogeneous: the azimuthal velocity component couples with the radial and streamwise ones. Such a streamwise-varying solution resembles that observed, both in the channel (Quadrio *et al.* 2009) and the pipe (Gallorini & Quadrio 2024), when STWs produce drag increase.

4. Localised turbulence

At $Re_b = 4900$, the controlled pipe flow generally resembles a conventional turbulent wall flow with modified (increased or decreased) friction. However, for certain control parameters, the flow becomes fully laminar and, more interestingly, sometimes exhibits spatially localised turbulence. In this section we focus on the localised turbulence state observed in a controlled pipe flow.

4.1. *Identification*

A criterion is needed to discriminate between space-filling turbulence and transitional, localised turbulence with puffs. In canonical pipe flow, several approaches exist to detect turbulent puffs. The instantaneous cross-plane turbulent kinetic energy $q(x, t)$, employed for instance by Moxey & Barkley (2010), is commonly used to detect puffs. The quantity $q(x, t)$ is defined as the sum of squares of the radial and azimuthal velocity fluctuations (indicated by the superscript $'$), over the cross-sectional plane with area A. This averaging operator is denoted by $\langle \cdot \rangle_A$:

$$q(x, t) = \frac{4}{\pi D^2} \int_0^{D/2} \int_0^{2\pi} \left({u'_r}^2 + {u'_\theta}^2 \right) r \, \mathrm{d}r \, \mathrm{d}\theta = \left\langle {u'_r}^2 + {u'_\theta}^2 \right\rangle_A. \tag{4.1}$$

The flow exhibits streamwise modulation due to the forcing in the azimuthal component. To mitigate it, the forced harmonic is removed from the fluctuating field.

The streamwise evolution of q for parameters $k^+ = 0.0126$ and $\omega^+ = 0.08$ (case I of table 1, with a large drag reduction of $\mathcal{R} = 31\,\%$) is shown in figure 4, along with a visualisation of the corresponding instantaneous turbulent structures. Using the λ_2 criterion (Jeong & Hussain 1995), these vortical structures appear as three localised clusters, separated by quiescent regions where turbulent fluctuations are significantly weaker. Correspondingly, $q(x)$ peaks at the centre of the clusters and gradually decreases to nearly zero in the gaps between adjacent clusters. In quiescent regions, minor oscillations persist due to imperfect forcing removal; nonlinearity transfers energy to higher harmonics.

To quantify localisation across all cases, $q(x, t)$ must be compressed into a single metric. Several alternatives have been tested, finding that the variability of q along the streamwise

https://doi.org/10.1017/jfm.2026.12073 Published online by Cambridge University Press

Case	k_x^+	ω^+	$\mathcal{R}$	n	L/D	$\langle q\rangle_p/U_b^2$	$\langle R^+\rangle_p$	U_u/U_b	U_d/U_b
A	6.3×10^{-3}	4×10^{-2}	40	1	9.9	1.5×10^{-2}	150	1.37	1.38
B	7.3×10^{-3}	4×10^{-2}	43	1	9.5	1.3×10^{-2}	148	1.40	1.40
C	8.4×10^{-3}	6×10^{-2}	28	3	5.4	1.1×10^{-2}	151	1.15	1.15
D	9.4×10^{-3}	6×10^{-2}	35	2	6.2	1.2×10^{-2}	150	1.29	1.24
E	1.05×10^{-2}	6×10^{-2}	37	2	6.1	1.1×10^{-2}	146	1.25	1.25
F	1.15×10^{-2}	6×10^{-2}	44	1	9.1	1.1×10^{-2}	143	1.38	1.35
G	1.15×10^{-2}	8×10^{-2}	27	3	5.7	1.0×10^{-3}	144	1.10	1.15
H	1.26×10^{-2}	6×10^{-2}	43	1	8.4	8.7×10^{-3}	141	1.37	1.43
I	1.26×10^{-2}	8×10^{-2}	31	3	4.9	9.9×10^{-3}	148	1.12	1.13
L	1.29×10^{-2}	8.6×10^{-2}	29	3	5.5	1.0×10^{-2}	149	1.13	1.12
M	1.36×10^{-2}	8×10^{-2}	33	3	4.8	8.8×10^{-3}	144	1.10	1.11
N	1.47×10^{-2}	8×10^{-2}	36	2	6.3	8.0×10^{-3}	143	1.29	1.15
O	—	—	—	1	5.0	1.1×10^{-2}	88	0.96	0.95

Table 1. Characteristics of the turbulent puffs for cases with localised turbulence: the set control parameters k_x^+ and ω^+, and the resulting drag-reduction rate $\mathcal{R}$, number of puffs n in the domain, length of the puffs L/D, cross-plane turbulent kinetic energy $\langle q\rangle_p$ and Kármán number $\langle R^+\rangle_p$ averaged within the puff volume, velocities of the upstream and downstream fronts U_u and U_d.

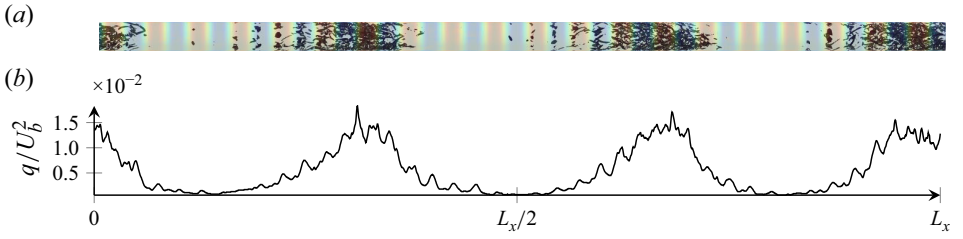


Figure 4. Instantaneous visualisation of localised turbulence along the pipe. The control parameters $k^+=0.0126$ and $\omega^+=0.08$ (case I of table 1) correspond to a large drag reduction of $\mathcal{R}=31\,\%$. (*a*) instantaneous configuration of the control (represented by the background colour, which indicates the azimuthal velocity of the wall) along with turbulence structures, visualised as isosurfaces of $\lambda_2^+=-0.06$. (*b*) evolution of q along the axial direction.

direction is best quantified by the indicator function $\mathcal{I}$, defined as the root-mean-square (r.m.s.) value σ_q of the space–time fluctuations of q over the entire time history, normalised by the bulk velocity squared:

$$\mathcal{I}=\frac{\sigma_q}{U_b^2}. \tag{4.2}$$

High values of $\mathcal{I}$ indicate spatially localised turbulence: when the flow contains alternating laminar and turbulent regions, $q(x)$ ranges from values close to zero in quasi-laminar zones to large values in the turbulent core of the puffs. Figure 5 shows a colour map of $\mathcal{I}$ as a function of the control parameters, with drag-reduction contours overlaid. High values of $\mathcal{I}$ occur at relatively low wavenumbers ($k_x^+<0.02$) and positive frequencies ($0<\omega^+<0.1$): spatially localised turbulence occurs mostly for forward-travelling waves. As expected, large drag reduction correlates with localised turbulence. However, the opposite is not true: large drag reduction does not necessarily imply localised turbulence. For instance, in much of the negative-frequency region, turbulence remains

https://doi.org/10.1017/jfm.2026.12073 Published online by Cambridge University Press

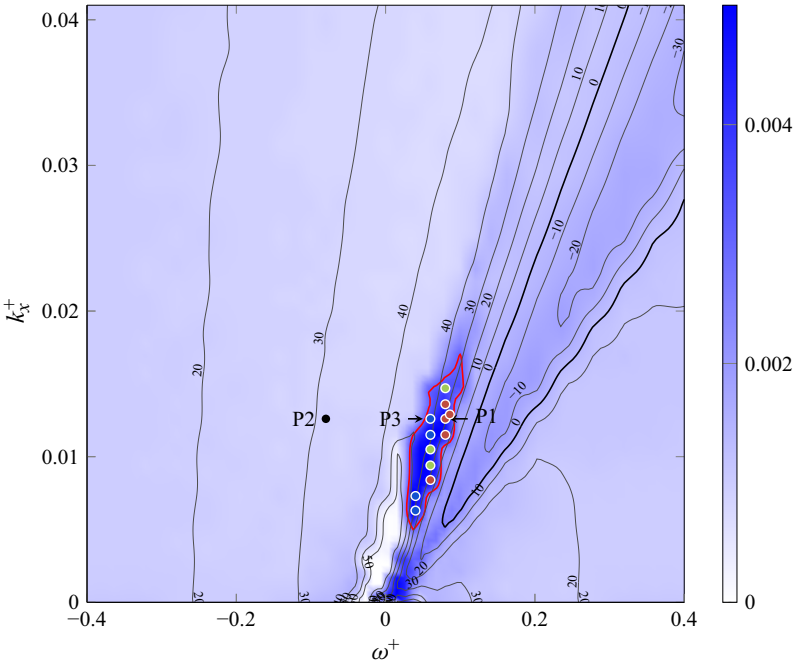


Figure 5. Map of the intermittency indicator $\mathcal{I}$ in the $\omega - k_x$ plane for $A^+ = 14.5$. Contours of $\mathcal{R}$, spaced by 10 % intervals, are overlaid to visualise the relation between $\mathcal{I}$ and drag reduction. The colour scale is saturated above $\mathcal{I} = 0.005$. The coloured dots indicate where localised turbulence is observed, with the number n of turbulent regions encoded by colour: $n = 1$ blue, $n = 2$ green and $n = 3$ red.

space-filling while drag reduction is large. Moreover, maximum $\mathcal{R}$ (corresponding to relaminarisation) yields very low $\mathcal{I}$ values.

We now examine three representative cases: P1, P2 and P3 in figure 5. Points P1 (at $\omega^+ = 0.08$, $k_x^+ = 0.0126$, case I in table 1) and P2 (at $\omega^+ = -0.08$, $k_x^+ = 0.0126$) produce the same drag reduction $\mathcal{R} = 31$ %. Their wavenumber is identical and their frequencies are opposite, yet their flow states differ: localised turbulence for P1 (downstream-travelling wave) and space-filling turbulence for P2 (upstream-travelling wave). The third point P3 (at $\omega^+ = 0.06$, $k_x^+ = 0.0126$, case H in table 1) has the same wavenumber and flow state (localised turbulence) as P1, but achieves a larger drag reduction, with $\mathcal{R} = 43$ %.

Figure 6 is a spatio-temporal plot of the function $q(x, t)$ for the three cases, all starting from the same uncontrolled initial condition. The same quantity for the flow in the absence of a control, denoted as REF, is also reported for comparison. Such space–time representation has been often used to examine the characteristics of transitional turbulent puffs in the canonical pipe flow (Moxey & Barkley 2010; Avila *et al.* 2011). The puffs are observed in a convecting reference frame moving at speed $\mathcal{U}$. For P1 and P3, presenting localised turbulence, $\mathcal{U}$ is the mean convective velocity of the turbulent region; for P2 and REF, $\mathcal{U} = U_b$ as in Moxey & Barkley (2010).

After control is applied at $t = 0$, $q(x, t)$ undergoes a characteristic transient phase, already described by Ricco *et al.* (2012) for the friction level, where fluctuations initially drop, and the flow moves towards the laminar state. For P1 and P2, this is followed by another reverse transient ($20 < tU_b/D < 50$), during which friction bounces back and turbulent fluctuations reappear uniformly along the streamwise direction. Despite identical long-term drag, the two cases diverge immediately after this transient. For P1, q becomes

https://doi.org/10.1017/jfm.2026.12073 Published online by Cambridge University Press

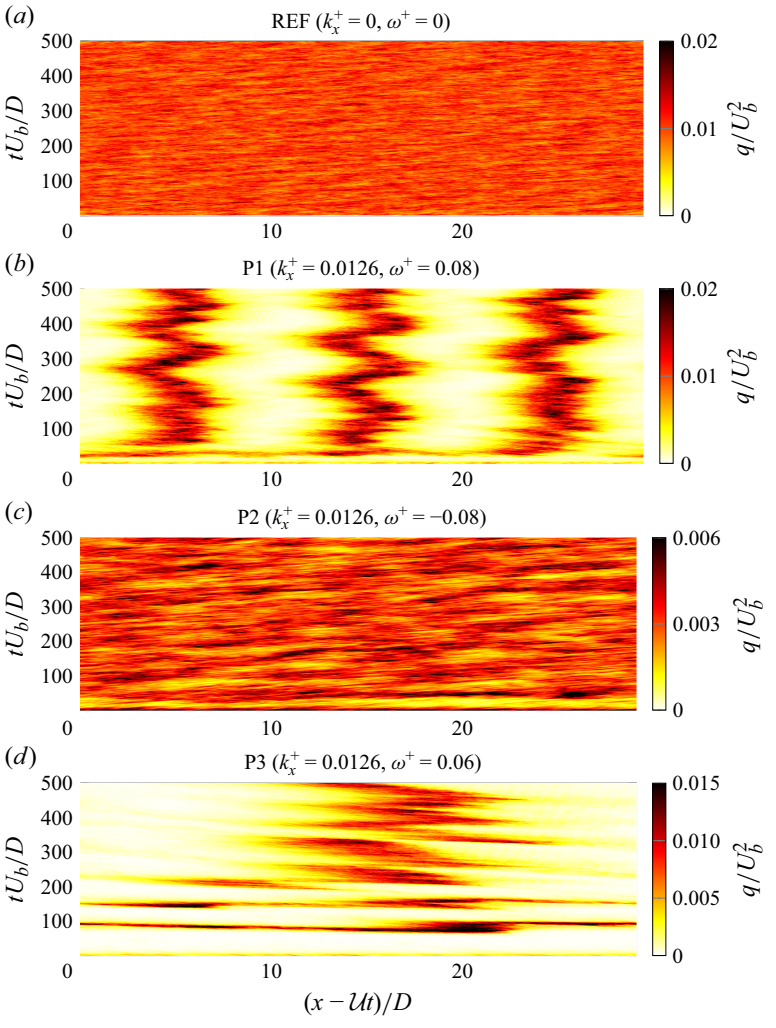


Figure 6. Space–time evolution of $q(x, t)$ for (*a*) REF, (*b*) P1, (*c*) P2 (*d*) and P3. Data are represented in the convecting reference frame at a speed $\mathcal{U}$: $\mathcal{U} = U_b$ for REF and P2, $\mathcal{U} = 1.12U_b$ for P1 and $\mathcal{U} = 1.4U_b$ for P3.

suddenly concentrated in three coherent spots of activity, which travel at an approximately constant velocity $1.12U_b$. These patches resemble canonical subcritical puffs (Avila *et al.* 2023); their properties will be analysed later in § 4.2. For P2, turbulence returns to its space-filling state after the transient, with no localisation, though intermittency is more pronounced than in the reference case. The space–time evolution of q for P3 is similar to P1, but with a single turbulent peak instead of three. After a relatively long transient, a single turbulent spot is established, moving at approximately $1.4U_b$.

The turbulent patches visible in the space–time maps of figure 6 resemble the well-documented puffs observed in transitional (canonical) pipe flows. However, $Re_b = 4900$ is more than twice the critical value $Re_c = 2040$ reported by Avila *et al.* (2011) for the uncontrolled flow as the critical point for the onset of sustained turbulence.

Observing localised puffs at such high Re_b, along with different flow states (laminar, localised, space-filling) at the same Re_b, shows that Re_b alone cannot characterise transition in controlled pipe flow. The same is true for a friction-based Reynolds number:

https://doi.org/10.1017/jfm.2026.12073 Published online by Cambridge University Press

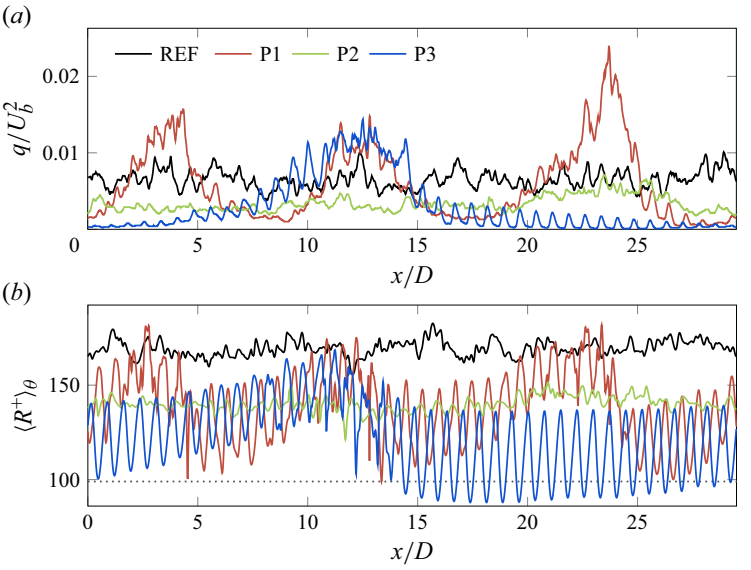


Figure 7. Streamwise distribution of (*a*) $q(x)$ and of (*b*) the azimuthally averaged wall friction for an instantaneous flow field far from the initial transient, for cases REF, P1, P2 and P3. The dotted line on panel (*b*) is R^+ for the laminar flow at $Re_b = 4900$.

P1 and P2 have the same value of the Kármán number R^+, but exhibit qualitatively different turbulence states (localised turbulence for P1 and space-filling turbulence for P2). As discussed for P1 and P3, the flow responds to the control by quickly decreasing friction and turbulent intensity. Before complete laminarisation, turbulence bounces back and re-intensifies sufficiently to trigger localised turbulence. The control thus drives the flow into a state that resembles canonical transitional conditions. In this state, space-filling turbulence can no longer be sustained, but survives only in spatially localised patches, where it is so intense that the overall friction is comparable to that of controlled pipes with fully developed (but attenuated) turbulence. A similar effect has been obtained by Barkley *et al.* (2015) at a comparable Reynolds number by adding a body force to blunt the shear profile. The initial decrease of Re_τ observed with STWs suggests that this control also produces a transient phase in which the near-wall shear is dramatically decreased. However, the interaction between the flow and the additional spanwise control gives rise to a velocity profile that, even at fixed k_x and ω, changes with space and time, thus triggering different responses to the flow disturbances, eventually resulting in a different flow state for different forcing parameters.

The streamwise distribution of q is shown in figure 7 for REF, P1, P2 and P3, for a generic flow field extracted at the latest stages of the simulations, when the flow has already assumed its long-term configuration. As expected for fully developed turbulence, the reference case shows a non-uniform value of q, which randomly oscillates around its mean value. The controlled cases differ markedly: P1 and P3 show localised peaks and troughs, while P2 exhibits no localised clustering. The turbulent clusters in P1 span approximately $5D$. The single turbulent cluster visible in P3 has an intensity comparable to P1, but a longer streamwise extension ($\sim 10D$), which aligns with information available on structures detected in the canonical case (Willis & Kerswell 2007; Avila & Hof 2013). In figure 7(*b*) we plot the streamwise evolution of the longitudinal wall friction, quantified via the local value $\langle R^+ \rangle_\theta(x)$ of the Kármán number defined in § 3. Unlike earlier analysis, the control harmonic is retained here to preserve friction modulation.

https://doi.org/10.1017/jfm.2026.12073 Published online by Cambridge University Press

Notably, the modulation is visible only for cases with localised turbulence, whereas P2, with space-filling turbulence, exhibits only small fluctuations around its mean value of $\langle R^+ \rangle_\theta \approx 140$. In contrast, P1 and P3 with localised turbulence present an evolution of $\langle R^+ \rangle_\theta$ that follows that of q (with a small spatial lag): maxima of $\langle R^+ \rangle_\theta$ correspond to clusters of turbulent activity and minima fall below the laminar value.

The following sections examine puff properties, using the operator $\langle \cdot \rangle_p$, which operates spatial averaging only across the region occupied by a puff. First, we must distinguish turbulent from laminar regions. The axial extent of each puff is extracted from $q(x, t)$ via a thresholding procedure: a position x is considered within a puff when $q(x) > q_t = 3.5 \times 10^{-3} U_b^2$. Though arbitrary, this threshold satisfies $q_t > q$ in laminar regions, while remaining sufficiently below the maximum in the turbulent core to prevent false positives induced by natural fluctuations; see figure 7. Appendix B describes how choosing q_t within a reasonable range does not alter the number of puffs and their propagation velocity. The thresholding criterion is complemented by the requirement that a region with $q > q_t$ must be connected and longer than $L_t = 3D$ to be considered a puff. The value L_t is selected after considering the probability density function (PDF) of the length of the extracted regions with $q > q_t$: as discussed in detail in § 4.2, the PDF is bimodal, with two evident and separated peaks centred around L_t, where the PDF is nearly zero.

4.2. *Characterisation*

The turbulent puffs observed in the controlled pipe flow present the same key features of the canonical structures: they maintain their spatial coherence for a long time, are surrounded by quiescent fluid and travel at a nearly constant speed. However, at the present large Reynolds number, no decay of the structures is observed. Indeed, it is known that the decay time increases exponentially with the Reynolds number (Hof *et al.* 2006), and here $Re_b = 4900$ is more than twice the typical value of subcritical uncontrolled pipe flows. At any rate, after the initial transient, puffs do not grow either; besides travelling, they do occasionally interact through merging and splitting, similarly to the uncontrolled puffs observed by Moxey & Barkley (2010) at $Re_b \sim 2300$.

We now provide a quantitative description of the puffs in the controlled pipe flow to ascertain to what extent their features align with those of the canonical puffs and whether they scale in inner or outer units. Table 1 reports several characteristics, computed over a time window of $tU_b/D = 250$, for a subset of cases in the entire database where coherent puffs remain clearly visible throughout the observation period and for which flow and control properties vary smoothly. This subset is delimited in figure 5 with the red contour and different cases represented with dots, whose colour encodes the number n of structures present in the domain. The table describes each case in terms of its control parameters, the value of $\mathcal{R}$, the number n, the average spatial extent L of each puff and the value of several puff-specific quantities. Case O (last row) represents canonical transitional puffs. This case is computed by following the procedure described by Moxey & Barkley (2010): starting from a fully developed turbulent field at $Re_b = 4900$, the Reynolds number is gradually reduced to $Re_b = 2200$, where a single turbulent puff is obtained. Specifically, Re_b is reduced in three discrete steps, with simulations advanced for $tU_b/D = 125$ for the first two steps and $tU_b/D = 375$ for the last one (statistics are extracted for the last $tU_b/D = 250$ units).

The quantity L in table 1 is the mean streamwise extension of the turbulent region. It is computed by integrating the PDF of the length l of the extracted turbulent regions for $l > L_t$, $PDF(l > L_t)$, i.e. only considering the events longer than the threshold length defined in § 4.1). Avila & Hof (2013) demonstrated that in pipe flow with localised

https://doi.org/10.1017/jfm.2026.12073 Published online by Cambridge University Press

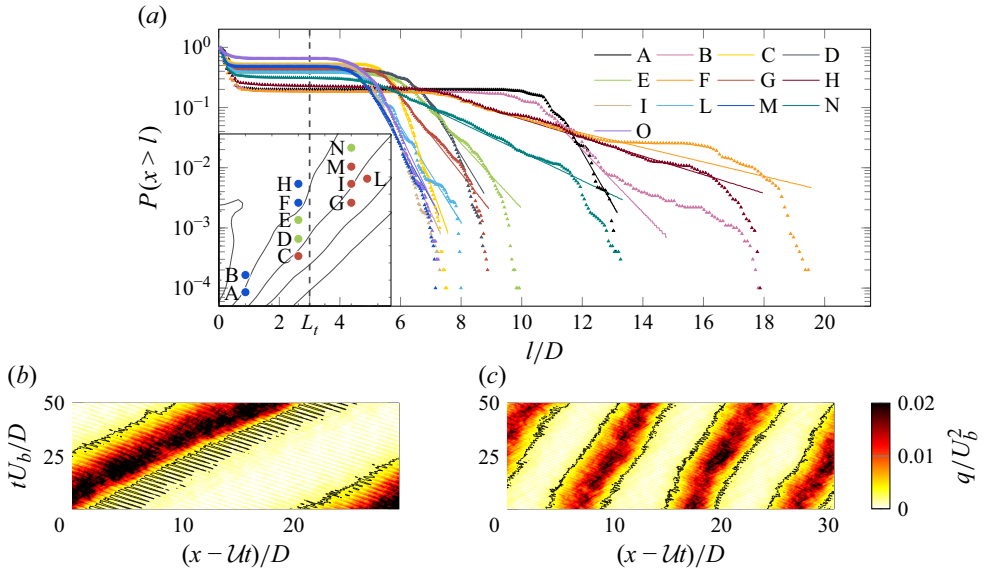


Figure 8. (*a*) Cumulative distribution function (CDF) of the puff length for cases listed in table 1. Continuous lines are the exponential distribution given by (4.3). The inset shows the positions of the different cases within the control parameter space, using the same symbols as in figure 4. (*b*,*c*) Space–time evolution of $q(x, t)$ for cases B (*b*) and I (*c*). The contour $q = q_t$ marks the spatial extension of the events. Here $\mathcal{U} = U_b$.

turbulence, the length of the spatio-temporally intermittent turbulent region exhibits exponential decay beyond a certain threshold $L_0 > L$ (different from the threshold value L_t used to discard small structures). This exponential decay characterises spatio-temporal intermittency, previously reported for other types of flow (Chaté & Manneville 1988; Ciliberto & Bigazzi 1988). We conduct a similar analysis to distinguish controlled and canonical puffs. The cumulative distribution function (CDF) of the puff length is first computed. Figure 8(*a*) shows the CDF for the cases listed in table 1. For very small lengths, say $l/D < 1$, the CDF suddenly drops from the unitary value, reflecting the presence of short spurious turbulent regions. Then the CDF levels off, indicating that no puffs exist in this range. The threshold value $L_t = 3D$ has been selected to always be within the plateau. At longer lengths, the CDF decreases again in correspondence with the shortest puffs. The shape of the CDF for all the cases reveals, therefore, very small turbulent regions ($l/D < 1$) as well as the longer structures identified as puffs. Turbulent regions of intermediate length are absent, showing a clear bimodal PDF. Moreover, the second decay of the CDF follows an exponential law (a straight line in the plot). To corroborate this observation, in figure 8 the various datasets are accompanied by an exponential distribution

$$CDF(l) = 1 - \mathrm{e}^{-(l-L_0)\lambda}, \tag{4.3}$$

where L_0 is the length scale (larger than the mean length of the puffs, according to Avila & Hof 2013) at which the CDF starts to exhibit exponential behaviour and the decay-rate parameter λ is obtained by fitting the data. The distributions exhibit exponential decay over a wide range of lengths, with gradual deviations appearing only for the longest events. Such deviations were not observed by Avila & Hof (2013) and could be related to the confinement of the finite domain, which could impact their statistical distribution, even though the robustness analysis reported in Appendix A.1 confirms a minor impact of the domain size on the mean properties of the structures. Cases B and F stand out and show a

https://doi.org/10.1017/jfm.2026.12073 Published online by Cambridge University Press

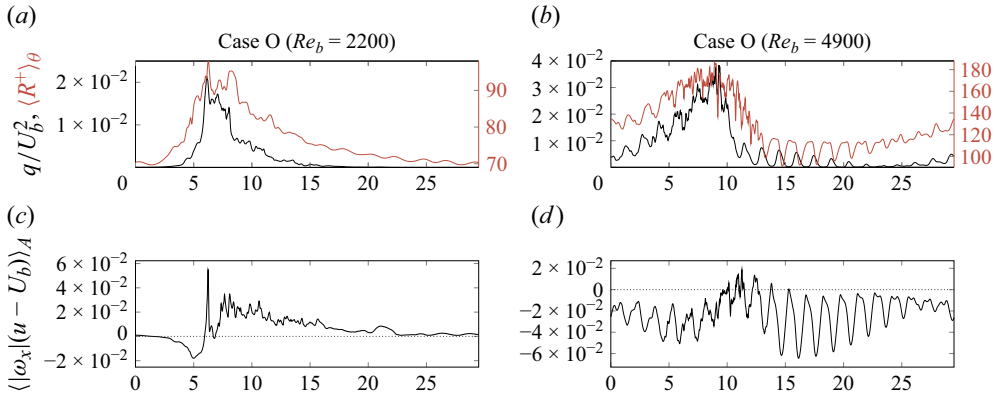


Figure 9. Comparison between uncontrolled (case O; panels *a,c*) and controlled (case A; panels *b,d*) puffs. For a single flow field, panels (*a,b*) show plots of $\langle R^+\rangle_\theta$ and q along the pipe at fixed time, and panels (*c,d*) show plots of the quantity $\langle|\omega_x|(u - U_b)\rangle_A$.

distinct behaviour, with a substantially slower decay than the exponential fit at intermediate lengths, before the final dropoff at large l. To understand this feature, in figure 8(*b,c*) we compare the space–time evolution of $q(x, t)$ for case B with one case showing a regular exponential decay (case I). The black contours indicate $q = q_t$. In case B, spikes emerge on the downstream (right) side of the puff, indicating that the control is not completely eliminated by zeroing the forced mode.

While the length is perhaps the most visible quantitative feature of the turbulent puffs, table 1 also contains the values $\langle q\rangle_p$ and $\langle R^+\rangle_p$ for the cross-plane turbulent kinetic energy q and the local friction Reynolds number R^+, averaged within the volume (or the pipe surface, respectively) occupied by the puff. The last columns report the velocities of the upstream and downstream fronts of the puffs, denoted as U_u and U_d. Most of the characteristics of the controlled puffs resemble those of the uncontrolled ones, including those of case O recomputed here. An exception is the much lower value of $\langle R^+\rangle_p$ for case O, which directly ensues from the lower Re_b of the uncontrolled pipe flow. Even though all controlled cases show large drag reduction and, therefore, a reduced R^+, the value of $\langle R^+\rangle_p$ remains much higher than that of the canonical puffs, namely $\langle R^+\rangle_p = 140 - 150$, compared with the value $\langle R^+\rangle_p = 88$ of case O. Another significant difference lies in the convection speed. The canonical puffs are slower than the bulk flow, with a convection speed of approximately 95 % of the bulk velocity, with $U_u/U_b = 0.94$ and $U_d/U_b = 0.96$, as reported in the literature and confirmed here for case O. On the contrary, under drag reduction, the puffs are found to travel much faster than U_b. For example, case B has $U_u/U_b = 1.47$ and $U_d/U_b = 1.43$.

To compare uncontrolled and controlled puffs, in figure 9 we plot the streamwise evolution of $\langle R^+\rangle_\theta$ and q for an instantaneous flow field, for cases O and A, both containing a single puff. Besides the obvious control-induced modulation, some qualitative differences exist in the turbulent regions. In the uncontrolled case, the upstream (left) front presents a steep increase of q from the laminar to the turbulent level, while the downstream (right) front exhibits a more gradual decay to zero. This asymmetry is a known property of the uncontrolled turbulent puffs (Hof *et al.* 2010). The controlled puffs exhibit the opposite behaviour, with a gradual rise of q upstream and a steep downstream front. This dissimilarity is confirmed by figure 9(*c,d*), plotting the streamwise evolution of the cross-sectional average of the quantity $\langle|\omega_x|(u - U_b)\rangle_A$, i.e. the streamwise vorticity (when computing vorticity, the control's harmonic is set to zero for case A) multiplied

https://doi.org/10.1017/jfm.2026.12073 Published online by Cambridge University Press

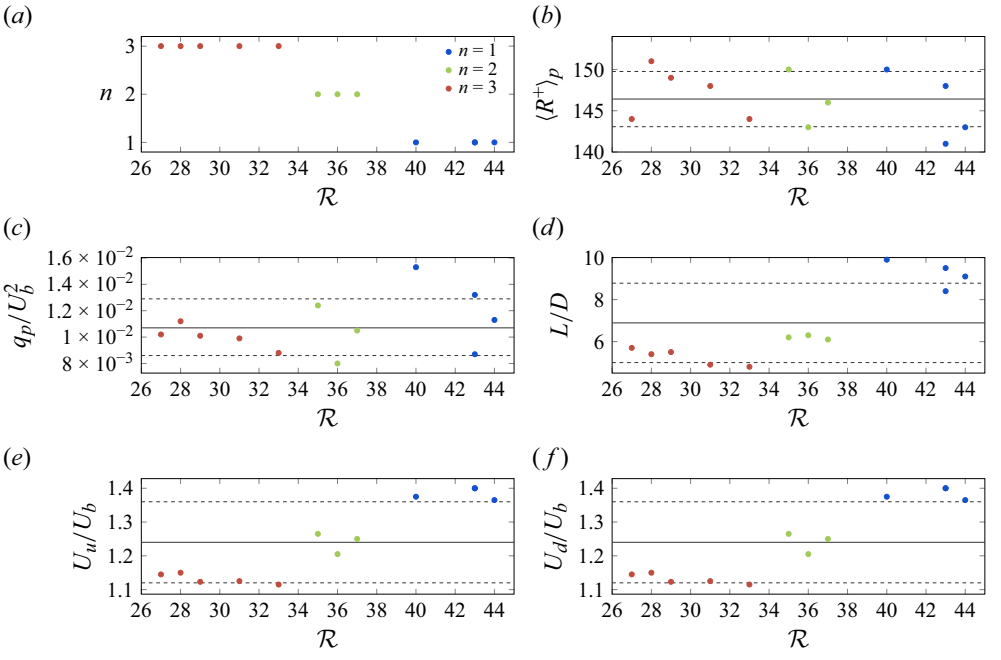


Figure 10. Relation between drag-reduction rate $\mathcal{R}$ and various quantitative features of the puffs, taken from table 1. The panels plot: (*a*) number of puffs in the computational domain; (*b*) average Kármán number within the puffs; (*c*) cross-plane turbulent kinetic energy $\langle q \rangle_p$ within the puffs, with inner/outer scaling; (*d*) puff length; (*e*, *f*) upstream and downstream front speed. The horizontal solid line indicates the mean value and the two dashed lines visualise the range of ± the r.m.s. value.

by the streamwise velocity relative to the bulk velocity. Hof *et al.* (2010) introduced this quantity to describe the streamwise rolls generated at the inflection point of the velocity profile in the puff, quantifying the magnitude of the vorticity transport. Here, $\langle |\omega_x|(u - U_b) \rangle_A$ is negative everywhere for case A, except for a small region at the downstream front, while it is positive everywhere for case O, except for a small region at the upstream front.

Figure 10 illustrates the relation between various quantities extracted from table 1. The number n of puffs observed in the computational domain correlates with $\mathcal{R}$. When $n = 1$, drag reduction is large (above 40 %). For $n = 2$, $35\,\% < \mathcal{R} < 38\,\%$, while for $n = 3$, $\mathcal{R}$ assumes lower values. In the dataset considered here, at most three puffs are observed. For even smaller $\mathcal{R}$, conventional space-filling turbulence develops and puffs disappear.

The friction Reynolds number $\langle R^+ \rangle_p$ within the puff does not correlate with n and $\mathcal{R}$, and hovers in the range 145–150 with a r.m.s. variation of only 2 % of the mean value, indicating that different levels of global drag reduction must derive from the different spatial extent of the laminar region between puffs. The puff intensity, quantified by $\langle q \rangle_p / U_b^2$, varies across cases. Expressing it in inner or outer units does not reveal any clear scaling. The r.m.s. variation is about 19 % of the mean value, with a tendency to increase for the lowest n. In contrast, both the puff length and the upstream and downstream front speeds U_u and U_d decrease with n, as seen from figure 10(*e*,*f*). Note that U_u and U_d always take similar values, implying that the puffs neither spread nor merge, but retain their spatial coherency.

https://doi.org/10.1017/jfm.2026.12073 Published online by Cambridge University Press

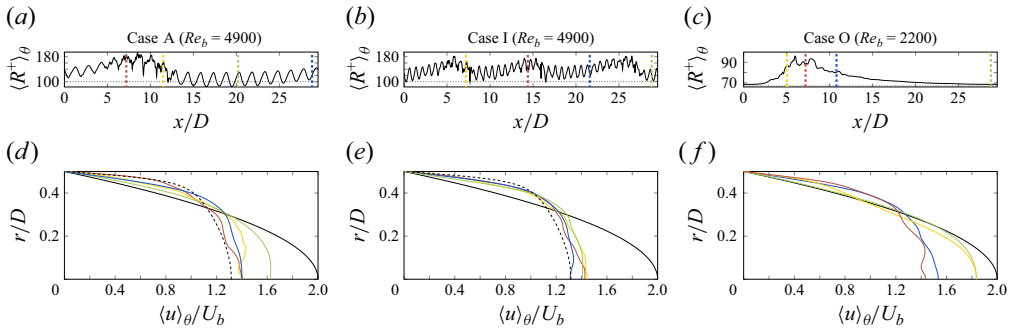


Figure 11. (*a–c*) Local friction Reynolds number and (*d–f*) azimuthally averaged axial velocity profile for case A with $n = 1$ (*a,d*), case I with $n = 3$ (*b,e*) and the uncontrolled case at $Re_b = 2200$ (*c,f*). In panels (*a–c*) the horizontal dotted line indicates the laminar value. The profiles in panels (*d–f*) are extracted at axial positions marked by vertical dashed lines with matching colours in (*a–c*). The black solid lines represent the velocity profile for laminar Hagen–Poiseuille flow, while the dashed lines for cases A and I represent the mean velocity profile in the uncontrolled case.

Scaling in inner units, i.e. using the friction velocity of the drag-reduced flow u_τ and viscous length δ_ν does not collapse the data. For $\langle q \rangle_p$ and U_m, which increase in outer units with $\mathcal{R}$, inner scaling accentuates these variations. Even for the puff length, which decreases with $\mathcal{R}$, the dispersion of the values around the mean is only slightly reduced.

Note that typical values of U_m^*, where $U_m = (U_u + U_d)/2$, are between 20 and 30, i.e. higher than the phase speed of the forcing (maximum value ∼6.5). Here U_m^* is also larger than the typical convection velocity of near-wall coherent structures in a fully developed wall-bounded turbulent flow (∼10). The puffs therefore substantially differ from canonical near-wall structures and propagate at velocities that differ significantly from the local bulk speed. Therefore, although for this subset of cases the level of $\mathcal{R}$ does affect the state of turbulence and links with the number, size and front convection speed of the puffs, no clear relationship emerges between $\mathcal{R}$ and the turbulence intensity within a puff.

The localised turbulent regions vary widely with k_x and ω. While sharing their intermittent character with canonical transitional puffs, they exhibit marked differences, possibly hinting at a distinct physical nature. However, all structures evolve coherently without exhibiting slug-like behaviour, splitting or decay, conversely suggesting a unified underlying mechanism. The canonical transitional structures and the localised states investigated here can be considered as members of the same family, whose properties are dynamically modulated by the control input.

4.3. *Radial structure of the puffs*

Since global features of the puffs exhibit neither inner scaling, where the velocity scale is derived from the wall slope of the axial profile, nor outer scaling, where the velocity scale is determined by the core region, it is of particular interest to examine the radial distribution of the statistical properties of the flow.

The instantaneous axial velocity profile is known to exhibit significant variability along the axial direction for canonical puffs (Avila & Hof 2013). The axial evolution is shown in figure 11, by considering three cases: case A with $n = 1$ and $\mathcal{R} = 40\,\%$ (panels *a,d*), case I with $n = 3$ and $\mathcal{R} = 31\,\%$ (panels *b,e*) and the uncontrolled case O with $n = 1$ at $Re_b = 2200$ (panels *c,f*). In panels (*a–c*) we plot the local $\langle R^+ \rangle_\theta(x)$, after removing the control harmonic. Panels (*d–f*) illustrates the local axial velocity profile $\langle u \rangle_\theta(r)$, extracted from an instantaneous snapshot, azimuthally averaged, and plotted at different

https://doi.org/10.1017/jfm.2026.12073 Published online by Cambridge University Press

axial locations representing the mild (blue) and steep (yellow) fronts of the puff. Profiles extracted from the region of most intense turbulent activity (red) and within the laminar plateau (green) are also shown. The laminar parabolic profile at the same flow rate (black) is plotted for reference, together with the uncontrolled turbulent velocity profile for cases at $Re_b = 4900$.

When $n = 1$ (case A; figure 11*a*,*d*), the local friction within the turbulent spot reaches a maximum of $\langle R^+ \rangle_\theta \approx 180$, which is slightly higher than that of the uncontrolled pipe flow at the same Re_b. The corresponding velocity profile (red), which exhibits slight oscillations because only azimuthal averaging is performed, resembles a typical turbulent profile, especially in the vicinity of the wall, with a nearly flat core and a steep near-wall gradient. Downstream of the position of maximum R^+, a recovery region is observed where the local friction decreases. The velocity profile (yellow) approaches the parabolic one: the flat central region is still discernible but becomes narrower, and near the wall, the profile is quite close to the parabolic one. The laminar value of R^+ is reached at about $x/D \approx 20$, but the corresponding profile (green) does not fully recover the laminar profile. It still exhibits a rather flat bulk region with a centreline velocity of $\approx 1.6U_b$ (instead of the laminar value $2U_b$). For r/D between 0.3 and 0.5, the actual velocity exceeds the laminar value. Lastly, upstream of the plateau, the front region shows a progressive increase in R^+ up to its peak. The velocity profile (blue) approaches the turbulent one again, although with lower velocities near the wall.

When $n = 3$ (case I; figure 11*b*,*e*), the separation between adjacent turbulent regions is limited: the downstream side of one puff penetrates the upstream side of the next one. As a result, the local friction remains significantly higher than the laminar value across the entire length of the pipe. In contrast to the $n = 1$ case, the velocity profile exhibits minimal variations throughout the domain, including at the centreline. Even at the location where the local wall shear stress reaches its minimum, the velocity profile (green) remains similar to the others and quite far from the parabola.

The single puff at $Re_b = 2200$ (case O; figure 11*c*,*f*) is similar to the case with $n = 1$. The size of the turbulent puff is comparable, and the expected sharp upstream and mild downstream fronts are observed. Interestingly, the upstream (yellow) profile presents an inflection point similar to that observed by Hof *et al.* (2010). A closer look at the corresponding profiles for $n = 1$ (at $x/D = 11.5$) and $n = 3$ (at $x/D = 7.2$) suggests the presence of similar, although less evident, inflection points located at comparable wall distances.

In figure 12 we plot mean velocity profiles, normalised in inner and outer units, and compares different criteria for averaging. Panels (*a*,*b*) present the global mean $\langle u \rangle(r)$ and panels (*c*,*d*) show the puff-averaged profile $\langle u \rangle_p(r)$. Four controlled cases (namely A, D, F and I) with different values of n are considered and compared with the uncontrolled case O at $Re_b = 2200$: two cases have $n = 1$, while exhibiting qualitatively different puffs in terms of intensity and length; one case has $n = 2$ and one has $n = 3$. The mean turbulent velocity profile for the uncontrolled case at $Re_b = 4900$ is added as a reference.

The profile $\langle u \rangle(r)$ in the outer scaling (figure 12*a*) varies across the different cases, with the centreline velocity $\langle u \rangle(0)$ being the largest for the uncontrolled case O and decreasing with increasing n (and, therefore, with decreasing drag reduction), and reaching the minimum for the fully developed turbulent profile. Note, however, that the centreline velocity is not determined solely by $\mathcal{R}$, as $\langle u \rangle(0)$ is higher for case A with $\mathcal{R} = 40$ than for case F with $\mathcal{R} = 44$. Panel (*b*) shows the same profiles in the law-of-the-wall form with actual viscous scaling defined in § 2. The controlled cases collapse, as expected, near the wall, whereas they are quite scattered in the incipient logarithmic region, barely visible because of the low Re, with case F above O and the others below. All the controlled

https://doi.org/10.1017/jfm.2026.12073 Published online by Cambridge University Press

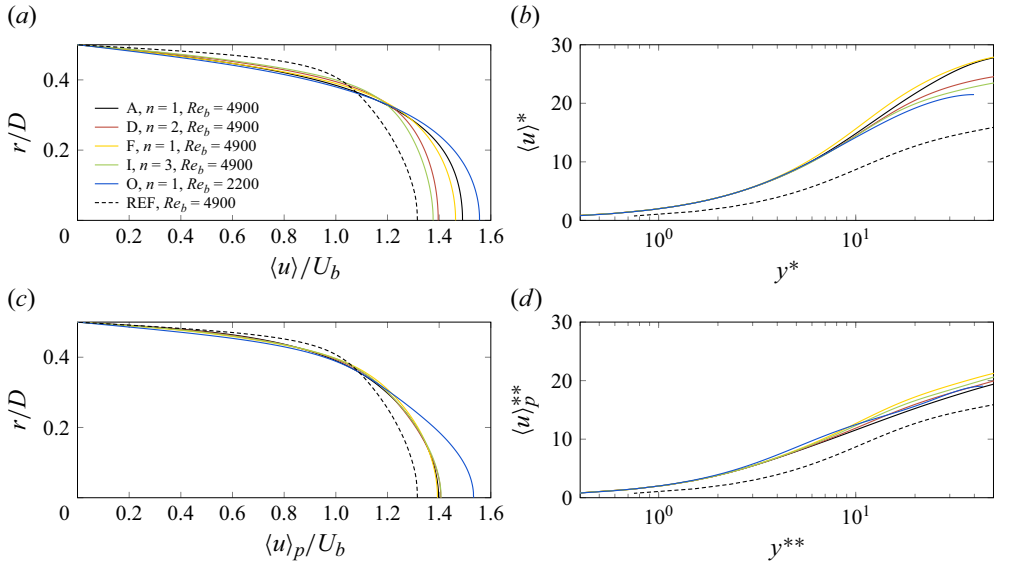


Figure 12. Mean velocity profiles in the (*a*,*c*) outer and (*b*,*d*) actual inner scaling. (*a*,*b*) Global mean profile $\langle u\rangle(r)$. (*c*,*d*) Mean profile $\langle u\rangle_p(r)$ averaged only over the puffs. The dashed lines represent the mean velocity profile for the uncontrolled case at $Re_b = 4900$.

profiles show an upward shift of the logarithmic region compared with REF, in agreement with the drag-reducing action of the control.

Despite the remarkable differences in the spatial arrangement of the puffs, all the puff-averaged profiles $\langle u\rangle_p(r)$ collapse in external units (panel *c*). The profile for the uncontrolled case O stands out. A lower wall gradient and, therefore, lower velocity levels in the near-wall region are expected, since $\langle R^+\rangle_p$ is smaller (see table 1). Therefore, since the flow rate is the same by design, velocities must be larger in the core. The maximum centreline velocity for O reaches $\langle u\rangle_p(0)/U_b \sim 1.53$, which is below the laminar value $\langle u\rangle(0)/U_b = 2$. For the controlled cases, a value $\langle u\rangle_p(0)/U_b \sim 1.4$ is observed. When the friction velocity is computed locally within the puff, such local inner scaling leads to the expected collapse of the various profiles in the near-wall region (panel *d*). However, owing to the limited variability of $\langle R^+\rangle_p$, the velocity profiles (including the uncontrolled case O) collapse quite well in the logarithmic region too.

In figure 13 we plot the radial distribution of the puff-averaged turbulent kinetic energy $\langle k\rangle_p$ (after removal of the forced mode), scaled in external units (panel *a*) and actual-local viscous units (panel *b*). This quantity differs from $\langle q\rangle_p$ since it includes fluctuations in the streamwise direction, in addition to a 0.5 prefactor. Also in this figure, the turbulent kinetic energy profile for the uncontrolled case at $Re_b = 4900$ is added as a reference. In general, apart from case F, when scaled in external units, the puffs are more energetic than the fully developed turbulent uncontrolled flow. The shape of the $\langle k\rangle_p$ profile for the uncontrolled case O presents two peaks of comparable intensity: one is close to the wall and a second, broader, towards the centreline. The controlled profiles are qualitatively different from O. The position of the near-wall peak of $\langle k\rangle_p$ is variable in outer units, but collapses to the canonical value of about 15 wall units when scaled in local viscous units. Looking at the shape of the profiles, two groups of curves can be identified. For cases A, F (and B, which is not shown), the turbulent kinetic energy peaks near the wall, then drops and flattens out up to far from the wall ($r/D \sim 0.2$, $y^* \sim 100$). This plateau is absent for the other cases,

https://doi.org/10.1017/jfm.2026.12073 Published online by Cambridge University Press

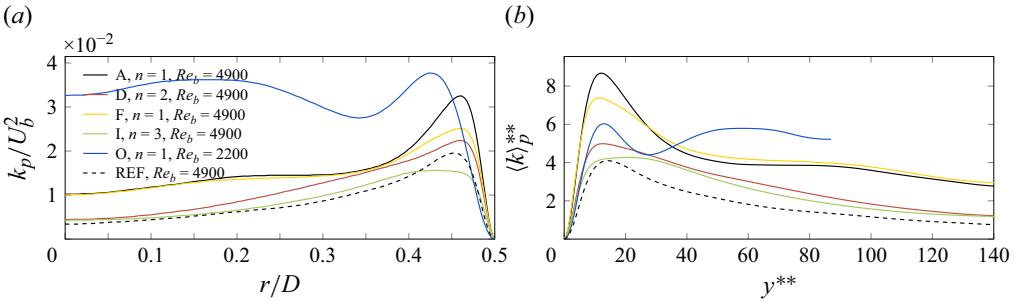


Figure 13. Radial distribution of the puff-averaged turbulent kinetic energy $\langle k\rangle_p$, scaled in (*a*) external and (*b*) actual viscous units. The dashed lines represent the turbulent kinetic energy profile for the uncontrolled case at $Re_b = 4900$.

independently of the value of n. Note that the structures associated with cases A and F are more energetic than the others, despite the level of drag reduction being substantially higher. This can be explained by the different number of structures n: for cases A and F, $n = 1$, meaning that despite the structures being more energetic, the overall friction is reduced due to the extended laminar or almost laminar recovery regions observed; see, for example, figure 7.

The previous observations provide insight into the internal structure of the controlled puffs. Their faster convection can in principle be related to faster near-wall structures, which shift in the wall-normal direction under STWs (Gallorini *et al.* 2022). However, the unchanged position of the peak in $\langle k\rangle_p$, shown in figure 13, rules out such a possibility. By contrast, the canonical case O at low Re presents a peak of $\langle k\rangle_p$ near the centre. In this case, the convective velocity of the puffs actually decreases (see table 1), indicating that the radial distribution of turbulent kinetic energy does not determine the propagation velocity of the puffs.

5. Concluding discussion

This work has studied the effect of streamwise-travelling waves of azimuthal velocity on a turbulent pipe flow at $Re_b = 4900$ using DNS. We have provided the first comprehensive drag-reduction map for the pipe geometry and investigated the subcritical turbulent state that develops in the controlled pipe.

Considering a pipe of length $30D$, we have examined how control parameters k_x and ω affect drag reduction at fixed amplitude $A^+ = 14.5$, including large-wavelength configurations. A drag-reduction map analogous to that available for plane channel flow (Quadrio *et al.* 2009) has been obtained. The comparison between the two geometries has highlighted that the pipe outperforms the channel in terms of maximum drag reduction $\mathcal{R}$ and net power saving $\mathcal{S}$. Notably, the controlled pipe relaminarizes, in contrast to the channel flow. However, the channel performs slightly better for several non-optimal combinations of k_x and ω.

Focusing on the turbulence state created by the control parameters, we have observed localised turbulent spots embedded in quiescent fluid; they resemble the puffs typical of the subcritical transition in an uncontrolled pipe flow. However, a crucial difference exists: in canonical pipe flow transition, turbulence becomes sustained and space-filling above a Reynolds number of $Re_b = 2600$ (Moxey & Barkley 2010), whereas the present Reynolds number is much higher at $Re_b = 4900$. Since wall-based control alters the relation between Re_b and Re_τ (or equivalently, the Kármán number R^+ for pipe flow), one

https://doi.org/10.1017/jfm.2026.12073 Published online by Cambridge University Press

might expect Re_τ to better describe the transition process. However, cases with identical R^+ but different controls exhibit different turbulent states. This demonstrates that Re_τ alone cannot characterise transition in the controlled flow; the control parameters play an essential role alongside Re_b.

A criterion based on local variance of velocity fluctuations has been introduced to discriminate spatially localised turbulence, enabling the identification of a subset of cases used to quantitatively study turbulent puffs. We have compared these puffs with those observed in the canonical pipe. Their lengths are comparable, but other properties differ significantly. Interestingly, uncontrolled puffs travel slower than U_b, whereas the controlled structures exceed U_b, with convection speed showing weak dependence on drag reduction.

In conclusion, a STW modifies pipe flow beyond the pure effect on the friction drag: it fundamentally alters transition onset and the structure of turbulence. Under high drag reduction, turbulence organises itself into localised patterns reminiscent of the uncontrolled flow at much lower Re. Neither Re_b nor Re_τ alone fully characterises the flow regime or predicts transition.

Future works should assess the generality of these findings across parameter space, examining the physical mechanisms underlying laminarisation and localised turbulence. Whether this behaviour is characteristic of pipe flow alone also remains unclear. To our knowledge, similar localised turbulence has not been observed for plane channel flow. However, in subcritical conditions, intermittent laminar–turbulent patterns appear in plane Poiseuille flow and other canonical flows, including plane Couette and Taylor–Couette configurations (Tuckerman *et al.* 2020). Interesting questions are whether such intermittent patterns appear when control is applied to these other geometries, and whether puff-like structures comparable to those observed here exist in geometries with similar transition behaviour (e.g. the square duct Takeishi *et al.* 2015). These results emphasise the importance of understanding how both active approaches, such as STWs, and passive techniques, like riblets or surface roughness, modify the turbulent state in the subcritical regime.

Acknowledgements. Simulations were performed thanks to the Swedish National Infrastructure for Computing (SNIC) at the NSC (Linköping University). Computing time has also been provided by the Italian supercomputing center CINECA under the ISCRA C project DWaves. DM acknowledges the financial support provided by the Knut and Alice Wallenberg Foundation. Preliminary results of this research were presented by EG at the European Drag Reduction and Flow Control Meeting (EDRFCM 2024) in Turin, Italy (Gallorini *et al.* 2024)

Funding. This research received no specific grant from any funding agency, commercial or not-for-profit sectors.

Declaration of interests. The authors report no conflict of interest.

Appendix A. Domain length and initial conditions

Experiments on turbulent puffs typically require extremely long domains to fully characterise the process (Avila *et al.* 2010). To keep the computational cost of this parametric study reasonable, the streamwise length of the pipe is fixed for the bulk of the numerical study at $L_x \simeq 30D$. The finite length of the periodic domain imposes confinement. The number of puffs that exist at a given time in a periodic domain is quantised to integer values. Initial conditions may also influence the flow state. Therefore, here we quantify how flow statistics are influenced by the domain length (as done, for example, by Chin *et al.* 2010) and by the initial conditions.

https://doi.org/10.1017/jfm.2026.12073 Published online by Cambridge University Press

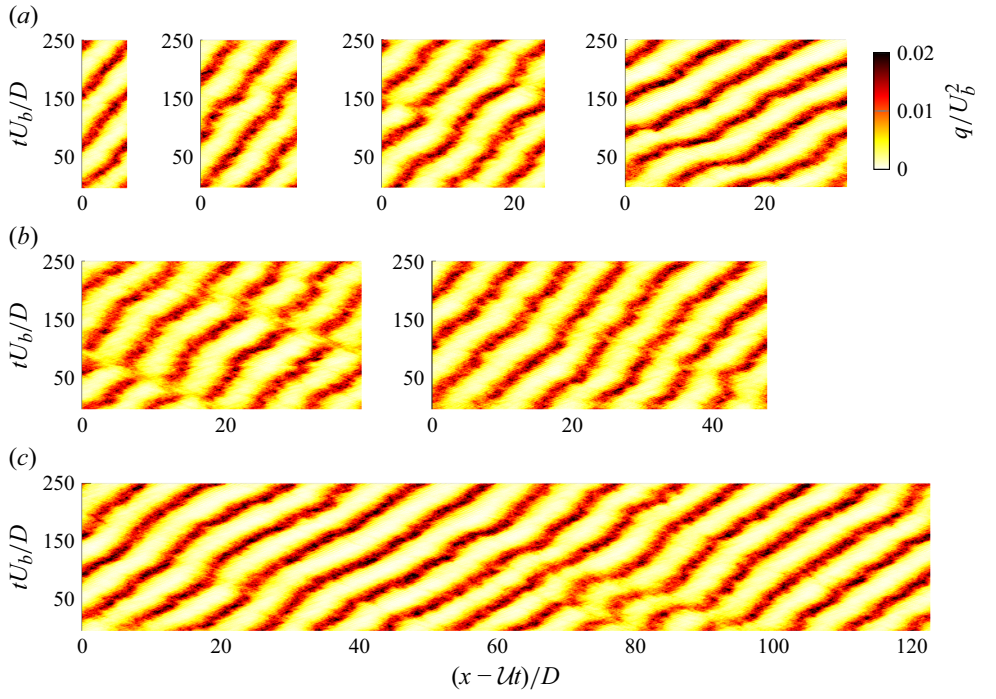


Figure 14. Space–time evolution of $q(x,t)$ (for the case with $k_x^+ = 0.0129$ and $\omega^+ = 0.086$) for different L_x: (*a*) $8.5D$, $15D$, $24.5D$, $32D$, (*b*) $39D$, $47.5D$ (*b*) and (*c*) $122.5D$.

A.1. *Effect of the domain length*

To explore quantisation effects, additional simulations are carried out. One case with localised turbulence ($k_x^+ = 0.0129$, $\omega^+ = 0.086$) is selected, and the pipe length is varied between $8.5D$ and $122D$, encompassing the baseline $L_x = 30D$ used in the main study. All other simulation parameters, including the spatial resolution, remain unchanged.

Results are summarised in table 2 in terms of $\mathcal{R}$ and its uncertainty $\delta\mathcal{R}$, computed as in Gatti & Quadrio (2016):

$$\delta\mathcal{R} = 100\frac{C_f}{C_{f,0}}\sqrt{\left(\frac{\delta C_f}{C_f}\right)^2 + \left(\frac{\delta C_{f,0}}{C_{f,0}}\right)^2}. \tag{A1}$$

Here δC_f and $\delta C_{f,0}$ are estimated using the procedure proposed by Russo & Luchini (2017). The relatively small changes of $\mathcal{R}$ with the domain length, together with the small uncertainties, suggest that the confinement effect does not significantly alter the extent of turbulent regions and, consequently, the value of drag reduction.

Figure 14 compares the space–time evolution of $q(x,t)$, as in figure 6 for the baseline cases. For consistency, $\mathcal{U} = U_b$ for all the cases. As expected, the number n of turbulent patches varies with the domain length, but the relationship between n and L_x is not straightforward. In the shortest domain with $L_x = 8.5D$, a single puff exists within the pipe. Doubling to $L_x = 16D$ produces $n = 2$. For $L_x = 24.5D$, $n = 3$ puffs are observed. As the domain length further increases, the number increases nonlinearly: $n = 3$ at $L_x = 32D$, $n = 5$ at $L_x = 39D$, $n = 6$ at $L_x = 47.5D$, up to $n = 13$ for the longest domain at $L_x = 122.5D$.

https://doi.org/10.1017/jfm.2026.12073 Published online by Cambridge University Press

L_x/D	8.5	16	24.5	32	39	47.5	122.5
$\mathcal{R}$	27.9	27.5	27.8	29.1	27.5	27.7	28.7
$\delta\mathcal{R}$	0.53	0.47	0.34	0.44	0.32	0.28	0.31
n	1	2	3	3	5	6	13
L/D	4.9	4.6	5.11	5.3	5.4	4.6	5.1
$\langle q\rangle_p/U_b^2$	9.1×10^{-3}	9.3×10^{-3}	8.5×10^{-3}	1×10^{-2}	8.2×10^{-3}	9.1×10^{-3}	0.98×10^{-3}
U_m/U_b	1.11	1.11	1.11	1.13	1.02	1.10	1.09
nD/L_x	0.116	0.126	0.122	0.095	0.128	0.126	0.106

Table 2. Dependence of $\mathcal{R}$, its uncertainty $\delta\mathcal{R}$ and characteristics of the turbulent regions (number n, length L, cross-plane turbulent kinetic energy $\langle q\rangle_p$, mean puff velocity U_m and number of puffs per unit length nD/L_x) with the domain length for the localised turbulence case with control parameters $k_x^+ = 0.0129$ and $\omega^+ = 0.086$.

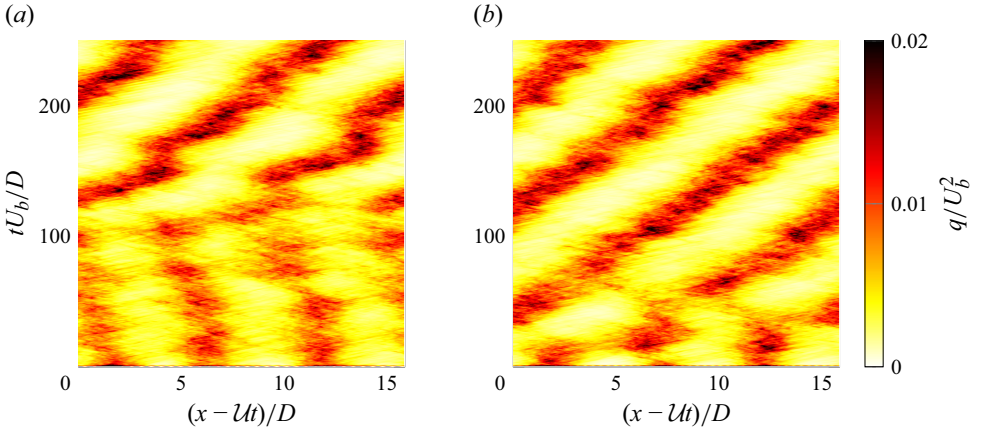


Figure 15. Space–time evolution of $q(x,t)$ (for the case with $k_x^+ = 0.0129$ and $\omega^+ = 0.086$) and $L_x = 16D$ with an initial condition originating from $L_x = 24.5D$ (*a*) and $L_x = 32D$ (*b*).

Figure 14 confirms that several features of the puffs are qualitatively affected by the domain length. In pipes with $L_x = 16D$ and $L_x = 47.5D$, the puffs are similar in length and intensity. In contrast, for $L_x = 32D$, they show greater extension and higher intensity, as quantified in table 2, which summarises the puff characteristics. In particular, the table reports the number n of puffs, their length L/D, their cross-plane turbulent kinetic energy $\langle q\rangle_p$, their mean convecting speed U_m, defined as the average of the upstream and downstream front velocities, and their number per unit length nD/L_x.

Overall, the domain length produces only minor variations in puff arrangement and intensity. The consistent drag-reduction values across all investigated scales confirm that confinement effects are negligible for the global flow behaviour.

A.2. *Effect of the initial conditions*

To test dependence on initial conditions, we performed two additional simulations at $L_x = 16D$, where $n = 2$ is expected (figure 14). Initial velocity fields were taken from simulations at $L_x = 24.5D$ and $L_x = 32D$ (both with $n = 3$), then interpolated onto the shorter domain while preserving the Fourier mode count. This creates a non-equilibrium initial condition that must adjust. Figure 15 shows $q(x,t)$ for the first $275U_b/D$ time units, with $\mathcal{U} = U_b$.

https://doi.org/10.1017/jfm.2026.12073 Published online by Cambridge University Press

Case	L/D	$\langle q\rangle_p/U_b^2$	$\langle R^+\rangle_p$	U_u/U_b	U_d/U_b	Case	L/D	$\langle q\rangle_p/U_b^2$	$\langle R^+\rangle_p$	U_u/U_b	U_d/U_b
A	7.3	1.8×10^{-2}	155	1.39	1.40	A	8.3	1.7×10^{-2}	151	1.39	1.38
B	7.0	1.6×10^{-2}	152	1.35	1.36	B	9.1	1.4×10^{-2}	148	1.43	1.44
C	3.7	1.4×10^{-2}	157	1.15	1.15	C	5.1	1.2×10^{-2}	152	1.13	1.12
D	4.4	1.5×10^{-2}	154	1.28	1.23	D	6.0	1.3×10^{-2}	151	1.25	1.26
E	4.1	1.3×10^{-2}	150	1.17	1.20	E	6.3	1.0×10^{-2}	146	1.23	1.20
F	6.1	1.4×10^{-2}	147	1.31	1.33	F	8.2	1.2×10^{-2}	143	1.32	1.38
G	3.7	1.3×10^{-2}	154	1.12	1.11	G	5.8	1.0×10^{-2}	152	1.16	1.12
H	4.6	1.2×10^{-2}	145	1.35	1.40	H	8.6	8.6×10^{-3}	138	1.37	1.42
I	3.2	1.2×10^{-2}	152	1.13	1.11	I	5.2	9.8×10^{-3}	147	1.12	1.11
L	3.7	1.3×10^{-2}	149	1.13	1.11	L	5.4	1.0×10^{-2}	152	1.13	1.12
M	2.9	1.1×10^{-2}	149	1.11	1.11	M	5.3	8.3×10^{-3}	142	1.10	1.11
N	3.9	1.0×10^{-2}	147	1.26	1.18	N	7.6	7.2×10^{-3}	141	1.15	1.22

Table 3. Quantitative characteristics of the localised turbulent regions for various threshold values q_t for the cross-plane turbulent kinetic energy. Left (columns 1–6): $q_t = 7\times10^{-3}U_b^2$. Right (columns 7–12): $q_t = 0.1q_{max}$.

Case	L/D	$\langle q\rangle_p/U_b^2$	$\langle R^+\rangle_p$	U_u/U_b	U_d/U_b
O	6.5	9.2×10^{-3}	87	0.96	0.95

Table 4. Quantitative characteristics of the localised turbulent regions in case O for a threshold value of $q_t = 2\times10^{-3}U_b^2$.

For both initial conditions, the number of structures in the domain eventually decreases from $n=3$ to $n=2$, indicating that the final turbulent state does not depend on the initial conditions for this case. The main statistical features remain nearly unaffected: the first case yields $\mathcal{R}=27.7\pm0.4$ and the second $\mathcal{R}=27.0\pm0.4$, compared with the reference value $\mathcal{R}=27.5\pm0.5$ (Appendix A.1). The transient behaviour differs, however. The simulation initialised with the shorter-domain solution exhibits a longer adjustment period during which three puffs persist, travelling at speeds below U_b. At $t\approx130$, rapid transition to the $n=2$ state occurs via coalescence, and the resulting structures immediately propagate faster than U_b. In contrast, the simulation from the longer-domain solution shows a much shorter transient with no evidence of structures moving slower than U_b.

Appendix B. Effect of the threshold value q_t on the quantitative features of the puffs

The characteristics of the puffs are affected by the choice of the threshold value q_t for the cross-sectional kinetic energy q, used to identify turbulent regions. Table 3 presents the same puff characteristics as table 1, computed for different threshold values. We consider $q_t = 7\cdot10^{-3}U_b^2$ (twice the baseline threshold), as well as a case-dependent threshold set at 10 % of the local maximum q. As expected, L, q_p and R_p^+ show variations with q_t, whereas U_u and U_d remain nearly constant. Front velocities exhibit the same correlation with $\mathcal{R}$, and all findings from § 4.2 are supported.

An additional consideration concerns the sensitivity of q_t to Re_b, discussed in § 4.2. Table 1 shows that case O at $Re_b=2200$ contains shorter structures than case A, despite both having $n=1$. Table 4 therefore reports puff properties for case O with a reduced

https://doi.org/10.1017/jfm.2026.12073 Published online by Cambridge University Press

threshold $q_t = 2 \times 10^{-3} U_b^2$, preserving the same ratio of q_t to peak kinetic energy as case A. The reduced q_t yields lower $\langle q \rangle_p / U_b^2$ and $\langle R^+ \rangle_p$ compared with table 1, while L/D increases. Again, front speeds are nearly insensitive to q_t. These results confirm that puffs in case O are shorter, weaker and slower than the $n = 1$ cases at $Re_b = 4900$, regardless of threshold choice.

References

Auteri, F., Baron, A., Belan, M., Campanardi, G. & Quadrio, M. 2010 Experimental assessment of drag reduction by traveling waves in a turbulent pipe flow. *Phys. Fluids* **22** (11), 115103–115114.

Avila, K., Moxey, D., de Lozar, A., Avila, M., Barkley, D. & Hof, B. 2011 The onset of turbulence in pipe flow. *Science* **333** (6039), 192–196.

Avila, M., Barkley, D. & Hof, B. 2023 Transition to turbulence in pipe flow. *Ann. Rev. Fluid Mech.* **55** (1), 575–602.

Avila, M. & Hof, B. 2013 Nature of laminar-turbulence intermittency in shear flows. *Phys. Rev. E* **87** (6), 063012.

Avila, M., Willis, A.P. & Hof, B. 2010 On the transient nature of localized pipe flow turbulence. *J. Fluid Mech.* **646**, 127–136.

Barkley, D., Song, B., Mukund, V., Lemoult, G., Avila, M. & Hof, B. 2015 The rise of fully turbulent flow. *Nature* **526** (7574), 550–553.

Berizzi, N., Gatti, D., Soldati, G., Pirozzoli, S. & Quadrio, M. 2025 Aerodynamic performance of a transonic airfoil with spanwise forcing. *J. Fluid Mech.* **1010**, A18.

Chaté, H. & Manneville, P. 1988 Spatio-temporal intermittency in coupled map lattices. *Physica D* **32** (3), 409–422.

Chin, C., Ooi, A.S.H., Marusic, I. & Blackburn, H.M. 2010 The influence of pipe length on turbulence statistics computed from direct numerical simulation data. *Phys. Fluids* **22** (115107), 1–10.

Ciliberto, S. & Bigazzi, P. 1988 Spatiotemporal intermittency in Rayleigh–Bénard convection. *Phys. Rev. Lett.* **60** (4), 286–289.

Coxe, D., Peet, Y. & Adrian, R. 2022 On Stokes' second problem solutions in cylindrical and Cartesian domains. *Phys. Fluids* **34** (10), 103615.

de Lozar, A. & Hof, B. 2009 An experimental study of the decay of turbulent puffs in pipe flow. *Phil. Trans. R. Soc. A* **367** (1888), 589–599.

Faisst, H. & Eckhardt, B. 2004 Sensitive dependence on initial conditions in transition to turbulence in pipe flow. *J. Fluid Mech.* **504**, 343–352.

Gallorini, E., Massaro, D., Schlatter, P. & Quadrio, M. 2024 The state of turbulence in a pipe flow with drag reduction. In *European Drag Reduction and Flow Control Meeting (EDRFCM) 2024, 10th - 13th September 2024 Turin (Torino), Italy*.

Gallorini, E. & Quadrio, M. 2024 Spatial discretization effects in spanwise forcing for turbulent drag reduction. *J. Fluid Mech.* **982**, A11.

Gallorini, E., Quadrio, M. & Gatti, D. 2022 Coherent near-wall structures and drag reduction by spanwise forcing. *Phys. Rev. Fluids* **7** (11), 114602.

Gattere, F., Zanolini, M., Gatti, D., Bernardini, M. & Quadrio, M. 2024 Turbulent drag reduction with streamwise-travelling waves in the compressible regime. *J. Fluid Mech.* **987**, A30.

Gatti, D. & Quadrio, M. 2016 Reynolds-number dependence of turbulent skin-friction drag reduction induced by spanwise forcing. *J. Fluid Mech.* **802**, 553–558.

Gatti, D., Quadrio, M., Chiarini, A., Gattere, F. & Pirozzoli, S. 2025 Turbulent skin-friction drag reduction via spanwise forcing at high Reynolds number. *J. Fluid Mech.* **1016**, A58, 1–23.

Hasegawa, Y., Quadrio, M. & Frohnapfel, B. 2014 Numerical simulation of turbulent duct flows at constant power input. *J. Fluid Mech.* **750**, 191–209.

Hof, B., de Lozar, A., Avila, M., Tu, X. & Schneider, T.M. 2010 Eliminating turbulence in spatially intermittent flows. *Science* **327** (5972), 1491–1494.

Hof, B., de Lozar, A., Kuik, D.J. & Westerweel, J. 2008 Repeller or attractor? Selecting the dynamical model for the onset of turbulence in pipe flow. *Phys. Rev. Lett.* **101** (21), 214501.

Hof, B., van Doorne, C.W.H., Westerweel, J. & Nieuwstadt, F.T.M. 2005 Turbulence regeneration in pipe flow at moderate Reynolds numbers. *Phys. Rev. Lett.* **95** (21), 214502.

Hof, B., Westerveel, J., Schneider, T. & Eckhardt, B. 2006 Finite lifetime of turbulence in shear flows. *Nature* **443**, 59–62.

Jeong, J. & Hussain, F. 1995 On the identification of a vortex. *J. Fluid Mech.* **285**, 69–94.

Kim, K.C. & Adrian, R.J. 1999 Very large-scale motion in the outer layer. *Phys. Fluids* **11** (2), 417–422.

https://doi.org/10.1017/jfm.2026.12073 Published online by Cambridge University Press

LEWIS, H.R. & BELLAN, P.M. 1990 Physical constraints on the coefficients of Fourier expansion in cylindrical coordinates. *J. Math. Phys.* **31** (11), 2592–2596.
LINDGREN, R. 1957 The transition process and other phenomena in viscous flow. PhD thesis, KTH Royal Institute of Technology.
LIU, X., ZHU, H., BAO, Y., ZHOU, D. & HAN, Z. 2022 Turbulence suppression by streamwise-varying wall rotation in pipe flow. *J. Fluid Mech.* **951**, A35.
LUCHINI, P. 2020 CPL. Available at: https://CPLcode.net.
LUCHINI, P. 2021 Introducing CPL. arXiv: 2012.12143v2.
LUCHINI, P. & QUADRIO, M. 2006 A low-cost parallel implementation of direct numerical simulation of wall turbulence. *J. Comput. Phys.* **211** (2), 551–571.
MASSARO, D., MARTINELLI, F., SCHMID, P.J. & QUADRIO, M. 2023 Linear stability of Poiseuille flow over a steady spanwise Stokes layer. *Phys. Rev. Fluids* **8** (10), 103902.
MESEGUER, Á. & TREFETHEN, L.N. 2003 Linearized pipe flow to Reynolds number 10ô7. *J. Comput. Phys.* **186** (1), 178–197.
MOXEY, D. & BARKLEY, D. 2010 Distinct large-scale turbulent-laminar states in transitional pipe flow. *PNAS* **107** (18), 8091–8096.
MUKUND, V. & HOF, B. 2018 The critical point of the transition to turbulence in pipe flow. *J. Fluid Mech.* **839**, 76–94.
PEIXINHO, J. & MULLIN, T. 2006 Decay of turbulence in pipe flow. *Phys. Rev. Lett.* **96** (9), 094501.
QUADRIO, M., FROHNAPFEL, B. & HASEGAWA, Y. 2016 Does the choice of the forcing term affect flow statistics in DNS of turbulent channel flow? *Eur. J. Mech. B/Fluids* **55**, 286–293.
QUADRIO, M. & RICCO, P. 2011 The laminar generalized Stokes layer and turbulent drag reduction. *J. Fluid Mech.* **667**, 135–157.
QUADRIO, M., RICCO, P. & VIOTTI, C. 2009 Streamwise-traveling waves of spanwise wall velocity for turbulent drag reduction. *J. Fluid Mech.* **627**, 161–178.
QUADRIO, M. & SIBILLA, S. 2000 Numerical simulation of turbulent flow in a pipe oscillating around its axis. *J. Fluid Mech.* **424**, 217–241.
RAI, M.M. & MOIN, P. 1991 Direct simulations of turbulent flow using finite-difference schemes. *J. Comput. Phys.* **96**, 15.
REYNOLDS, O. 1883 An experimental investigation on the circumstances which determine whether the motion of water shall be direct or sinuous, and the law of resistance in parallel channels. *Proc. R. Soc. Lond. A* **35**, 84.
RICCO, P., OTTONELLI, C., HASEGAWA, Y. & QUADRIO, M. 2012 Changes in turbulent dissipation in a channel flow with oscillating walls. *J. Fluid Mech.* **700**, 77–104.
RICCO, P. & QUADRIO, M. 2008 Wall-oscillation conditions for drag reduction in turbulent channel flow. *Intl J. Heat Fluid Flow* **29**, 601–612.
RICCO, P., SKOTE, M. & LESCHZINER, M.A. 2021 A review of turbulent skin-friction drag reduction by near-wall transverse forcing. *Prog. Aerosp. Sci.* **123**, 100713.
RUBY, M. & FOYSI, H. 2025 Effects by oscillation control and compressibility in supersonic turbulent channel flow. *Intl J. Heat Fluid Flow* **114**, 109820.
RUSSO, S. & LUCHINI, P. 2017 A fast algorithm for the estimation of statistical error in DNS (or experimental) time averages. *J. Comput. Phys.* **347**, 328–340.
SCHMID, P.J. & HENNINGSON, D.S. 2001 *Stability and Transition in Shear Flows*. Springer.
TAKEISHI, K., KAWAHARA, G., WAKABAYASHI, H., UHLMANN, M. & PINELLI, A. 2015 Localized turbulence structures in transitional rectangular-duct flow. *J. Fluid Mech.* **782**, 368–379.
TUCKERMAN, L., CHANTRY, M. & BARKLEY, D. 2020 Patterns in wall-bounded shear flows. *Annu. Rev. Fluid Mech.* **52** (2020), 343–367.
VAN DOORNE, C.W.H. & WESTERWEEL, J. 2008 The flow structure of a puff. *Phil. Trans. R. Soc. A* **367** (1888), 489–507.
WILLIS, A.P. & KERSWELL, R.R. 2007 Critical behavior in the relaminarization of localized turbulence in pipe flow. *Phys. Rev. Lett.* **98** (1), 014501.
WU, X. & MOIN, P. 2008 A direct numerical simulation study of the mean velocity characteristics in turbulent pipe flow. *J. Fluid Mech.* **608**, 81–112.
WYGNANSKI, I., SOKOLOV, M. & FRIEDMAN, D. 1975 On transition in a pipe. Part 2. The equilibrium puff. *J. Fluid Mech.* **69** (2), 283–304.
WYGNANSKI, I.J. & CHAMPAGNE, F.H. 1973 On transition in a pipe. Part 1. The origin of puffs and slugs and the flow in a turbulent slug. *J. Fluid Mech.* **59** (2), 281–335.
XIAO, M., CECI, A., ORLANDI, P. & PIROZZOLI, S. 2024 Direct numerical simulation of drag reduction in rotating pipe flow up to $Re_\tau \approx 3000$. *J. Fluid Mech.* **996**, A24.

https://doi.org/10.1017/jfm.2026.12073 Published online by Cambridge University Press